JGR Oceans

RESEARCH ARTICLE
10.1029/2024JC021021

Special Collection:
Physical processes, sediment transport and morphodynamics of estuaries and coastal seas

Observations of Mode-One Nonlinear Internal Waves (NLIW) of Opposite Polarity in Changing Background Conditions

A. Moncuquet[1], N. L. Jones[2], A. P. Zulberti[2], L. Bordois[3], F. Dufois[1], and P. Lazure[4]

[1]Institut Français de Recherche pour l'Exploitation de la Mer, DYNECO/DHYSED, Plouzané, France, [2]Oceans Graduate School and Oceans Institute, University of Western Australia, Perth, WA, Australia, [3]Service Hydrographie et Océanographie de la Marine, Brest, France, [4]Institut Français de Recherche pour l'Exploitation de la Mer, LOPS (UMR6523 CNRS/IFREMER/IRD/UBO), Plouzané, France

Abstract The transformation of internal waves on continental shelves is important to mass transfer, nutrient replenishment, and heat transfer. Yet, the transfer of energy from larger to smaller scale or between nonlinear internal waves (NLIW) themselves remains poorly understood. We present 1 month of through water column observations of temperature and currents on the southeast continental shelf of the Bay of Biscay, a region where internal wave dynamics have never been described. Over the shallower part of the shelf, a relatively strong baroclinic dynamic exists, with the mode-1 internal tide and NLIW generating currents more than three times the barotropic tide. The nature of these features varied greatly over the subtidal timescales, which we correlate to wind-driven currents and the associated modulation of background stratification. In addition to the well-documented processes of internal tide steepening and NLIW polarity reversal, we present novel observations of colocated elevation and depression (termed opposite polarity) NLIW. While this colocation has been previously studied theoretically, it has not been described with in situ observations to date. In agreement with theory, we observed these waves when the wind-driven dynamics resulted in double pycnocline stratification. We found that the collocated waves of depression and elevation propagate independently on the upper and lower pycnocline, respectively. We use direct estimates of wave speed to infer the potential for interaction between waves of opposite polarity and discuss the potential relevance for other regions worldwide where double pycnocline background conditions are observed.

Plain Language Summary Internal waves vertically displace surfaces of constant density (isopycnals). They can propagate long distances and reach continental shelves. High-frequency internal waves (with periods of few minutes) are usually termed nonlinear internal waves (NLIW). Coastal internal waves are a crucial driver of mixing between different ocean layers and cross-shelf transport all over the world. NLIW can displace isopycnals downward (depression waves) or upward (elevation waves). Internal waves propagate in a changing background environment, which affects their characteristics and, therefore, changes the mixing and transport they drive. In this study, we used temperature and velocity measurements to characterize the coastal internal waves between a period of 15 min and 12.42 hr (the semidiurnal tidal period) on the Bay of Biscay shelf. First, measurements indicate that internal waves at this location dominate the hydrodynamic forcing compared with the barotropic tide. We observe different internal waves depending on the background conditions. NLIW can displace isopycnals downward (depression waves) or upward (elevation waves). We have observed the coexistence of depression and elevation waves for the first time.

Key Points:

- Internal tides and nonlinear internal waves (NLIW) produce the strongest currents on the Aquitaine shelf
- Coastal wind-driven upwelling alters the cross-shelf evolution of the NLIW
- First field observations of coexisting mode-1 NLIW of opposite polarity under double-pycnocline conditions

Correspondence to:
A. Moncuquet,
Adele.Moncuquet@ifremer.fr

Citation:
Moncuquet, A., Jones, N. L., Zulberti, A. P., Bordois, L., Dufois, F., & Lazure, P. (2025). Observations of mode-one nonlinear internal waves (NLIW) of opposite polarity in changing background conditions. *Journal of Geophysical Research: Oceans*, *130*, e2024JC021021. https://doi.org/10.1029/2024JC021021

Received 1 AUG 2024
Accepted 9 JAN 2025

Author Contributions:
Conceptualization: A. Moncuquet, N. L. Jones, F. Dufois, P. Lazure
Data curation: F. Dufois, P. Lazure
Formal analysis: A. Moncuquet, P. Lazure
Funding acquisition: F. Dufois
Methodology: A. Moncuquet, A. P. Zulberti, L. Bordois, P. Lazure
Project administration: F. Dufois, P. Lazure
Resources: F. Dufois, P. Lazure
Supervision: N. L. Jones, A. P. Zulberti, L. Bordois, F. Dufois, P. Lazure
Writing – original draft: A. Moncuquet, N. L. Jones, A. P. Zulberti, L. Bordois, F. Dufois, P. Lazure
Writing – review & editing: A. Moncuquet, N. L. Jones, A. P. Zulberti, L. Bordois, F. Dufois, P. Lazure

1. Introduction

The transformation of the internal tide and nonlinear internal wave (NLIW) on the continental shelf is an important process in the transfer of ocean energy from large to small scales. Furthermore, internal tides and NLIW can dominate horizontal and vertical transport thereby impacting the sediment, nutrient, and pollutant distribution over the shelf (Cheriton, McPhee-Shaw, Shaw, et al., 2014; Molinas et al., 2020; Scotti & Pineda, 2004, 2007; Walter et al., 2012; Walter, Squibb, et al., 2014; Zhang et al., 2015; Zulberti et al., 2020). Identifying the types of internal waves observed over the continental shelf is the first step in understanding their impact on the continental shelf. The continental shelf is a shallow region in which a vast range of time and spatial scales dynamics are superimposed, for example, eddies, tidal currents and wind-induced currents (Csanady, 1981), leading to highly

variable background conditions (stratification, current, and water depth). These background conditions control the generation (Helfrich & Melville, 2006; Jackson et al., 2012) and evolution (Bai et al., 2021; Lamb, 2014; Shroyer et al., 2011) of internal waves on the continental shelf.

While NLIW may originate long distances from the shelf, in many cases they form or evolve locally (Jackson et al., 2012). A major generation mechanism on the inner shelf is the degeneration of long-period internal waves (e.g., semidiurnal tide or bores) through shoaling (Dauhajre et al., 2021; Walter et al., 2012). This evolution is highly sensitive to the bathymetric slope, the stratification, the subtidal currents, and the Coriolis force (Gerkema, 1996). Waves evolve slowly as they propagate long distances, and so, the offshore conditions are also important. Previous studies demonstrate the effect of background stratification and barotropic forcing on bore evolution (Dauhajre et al., 2021; Masunaga et al., 2019) as well as the near-inertial shear (Shroyer et al., 2011). Therefore, secondary flows such as offshore upwelling that alter the position of the pycnocline at the coast may influence tidal bore steepening at the coast (Walter, Woodson, et al., 2014).

Wave polarity is an important characteristic of NLIW. For mode-1 NLIW (i.e., the most common NLIW where all isotherms move in the same direction) *wave polarity* is defined by the depression/elevation of isotherms and the specific velocity pattern, that is, vorticity sign (Shroyer et al., 2009). Depression waves (downward isotherm excursion) are regularly observed in the open ocean where they can travel miles with no change of form (Ostrovsky & Stepanyants, 1989) and can reach continental shelves where they undergo various transformations (Grimshaw et al., 2004; Shroyer et al., 2009). Elevation waves (upward isotherm excursion and positive vorticity) are more commonly described on shallow or sloping continental shelves (Cheriton, McPhee-Shaw, Storlazzi, et al., 2014; Jones et al., 2020; Masunaga et al., 2019; McSweeney et al., 2020; Walter et al., 2012). Like the internal tide, NLIW can degenerate (break down) as they propagate. Common degeneration processes are polarity reversals as NLIW pass a *critical point* over the continental shelf (Shroyer et al., 2009) or generation of packets of waves of different polarities due to dissipation or interaction (Grimshaw et al., 2004).

Unlike the conventional description of (KdV) *solitons*, it has been numerically demonstrated that large NLIW interact, leading to energy transfer between the waves (Lamb, 2023), but these processes have not been well documented in situ. This is particularly true for NLIW of opposite polarity, the coexistence of depression and elevation waves, which has barely been described in situ in the oceanographic literature. These waves may be expected under double-pycnocline conditions, (Grimshaw et al., 2004; Lamb, 2023) which can result when upwelling drives cool water upslope forming a second near-bottom pycnocline (Cheriton, McPhee-Shaw, Storlazzi, et al., 2014). Given the prevalence of upwelling conditions and the significant energy transfer in theoretical results (Lamb, 2023), interactions of waves of opposite polarity may be an important undocumented process on the continental shelf.

In this paper, we describe the internal wavefield over the continental shelf of the Bay of Biscay (BoB) during July 2017, using in situ observations of the semidiurnal internal tide and mode-1 NLIW. The BoB is a hotspot for internal tide and NLIW generation (Baines, 1982; New & Pingree, 1992), but, so far, there are no in situ observations of internal waves on the shelf. Coastal NLIW of depression on the southeast (SE) continental shelf of the BoB have previously only been observed on a few satellite images (Jackson & Apel, 2002). In this contribution, (using 1 month of through water column observations of temperature and currents), we demonstrate how significant NLIW and internal tides are for the circulation of the SE BoB shelf. We highlight the key role of coastal wind-driven upwelling on the cross-shelf evolution of the NLIW. We compare the observations of NLIW polarity reversal with the observation of NLIW of opposite polarity, demonstrating for the first time the coexistence of mode-1 NLIW of opposite polarity in the ocean.

The paper is organized as follows. Section 2 presents the methodology. Section 3 is devoted to the description of the subtidal dynamics, the stratification, and the time evolution of the internal tide to give context for the NLIW described in Section 4. Two distinct internal spring tide regimes are highlighted, demonstrating the importance of the subtidal dynamics. Section 4 describes the evolution and details the dynamics of the NLIW packets. Four different types of NLIW packets are characterized, demonstrating the superposition of waves of opposite polarity. Summary and conclusions are provided in Section 5.

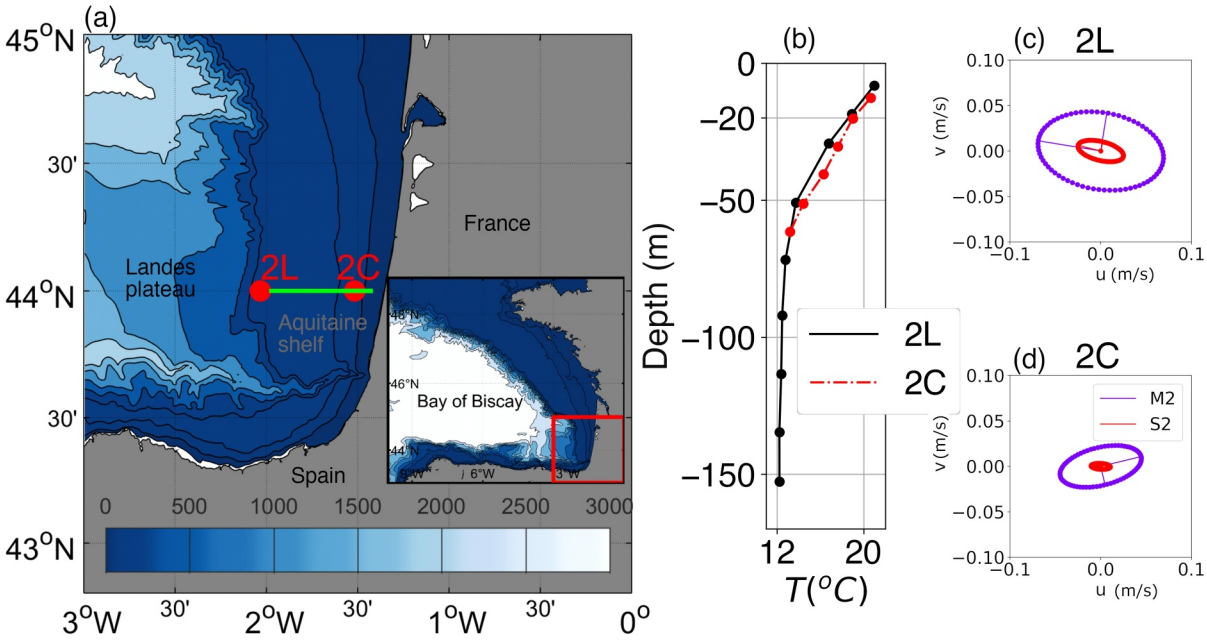

Figure 1. (a) Bay of Biscay (BoB) bathymetry around 44°N. The red points correspond to the outer-shelf mooring location 2L and inner-shelf mooring location 2C. The green line indicates the moving vessel profiler transect. A smaller portion of the transect is produced in Figure 7. The inset map is an extended view of the BoB. (b) Time-averaged temperature profile at the outer-shelf (solid line) and inner-shelf (dotted line). Red/black points show the time-averaged sensor depths in 2L/2C. (c, d) Barotropic tidal ellipse for M2 and S2 components at (c) the outer shelf and (d) inner shelf.

2. Methodology

2.1. Study Site

The BoB is located on the eastern side of the North Atlantic Ocean. The bay extends approximately 500 km meridionally from the Iberian Peninsula to the Celtic Sea (Figure 1a). The continental shelf width narrows toward the south along the French coast, from more than 200 km around 48°N to 30 km in the SE corner and along the Spanish coast (Figure 1a). The SE BoB is characterized by two shelf breaks that separate the shallow Aquitaine shelf, the deeper Landes plateau, and the abyssal plain. The first shelf break sits between 160 and 1,400 m, and the second shelf break ranges between 1,400 and 3,500 m (Figure 1a). In addition, numerous canyons cut through the shelf breaks, such as the "Gouf du Cap Breton," south of the study area (Figure 1a). These features are likely to increase the complexity of the dynamics.

The most energetic barotropic tides of the BoB are semidiurnal. The M2 maximum barotropic current is approximately 0.5 m/s at 45°N and decreases southward (Le Cann, 1990). From May to October, the temperature shows a marked seasonal cycle. The seasonal thermocline is stronger in the southern region, located around 30 m below the surface, deepens with time, and disappears in winter.

On the Aquitaine shelf, the barotropic current is less than 0.1 m/s at the study site, and the cross-shore component is dominant (Figures 1c and 1d). Barotropic, subtidal currents (seasonally averaged) are weak and generally poleward (Charria et al., 2013; Le Boyer et al., 2013). In summertime, the stratification is mainly modified by the wind-driven dynamics, alternating between local upwelling driven by northerly winds (Koutsikopoulos & LeCann, 1996; Puillat et al., 2004; Valencia et al., 2004) and the propagation of a downwelling circulation generated along the Spanish coast due to westerly winds. This subtidal poleward current is confined to shallow water (few internal Rossby radii, i.e., 5–10 km from the coast) and not observed deeper than 150 m depth (Batifoulier et al., 2012; Kersalé et al., 2016; Le Boyer et al., 2013).

As shown by Baines (1982), the BoB and Celtic shelf breaks are hot spots for internal wave generation. The internal tide and NLIW dynamics have been intensively studied for more than 40 years (Baines, 1982; New & Pingree, 1992; Pingree et al., 1986; Vlasenko & Stashchuk, 2015). Modeling studies have shown that internal waves are generated all along the continental slope within the BoB (Pairaud, 2005; Pichon et al., 2013). The first

Table 1
Moorings, Transect, and Instruments From the 2017 ETOILE Campaign

	1-month moorings (07–08 2017)						
Name	Instruments	δz (m)	Bottom height (m)	δt (s)	Latitude	Longitude	H (m)
2L	Mastodon—6 sensors	10; 20	0.7	60	43°59.9°N	2°02.537°W	153
2L	ADCP—300 kHz	2	4.5	2	44°00.1°N	2°01.5°W	153
2C	ADCP—300 kHz	1	4.5	2	44°00°N	1°31°W	62
2C	Mastodon—6 sensors	10	0.7	60	44°00°N	1°31°W	62

4 days (25–29/07 2017) MVP transects

Mounted sensors	δt (s)	Cross-shore distance traveled (km)	Maximal immersion (m)
CTD	0.04	[41–52]	[100–300]

Note. For the moorings: H is the total depth from pressure measured mean over time, δz is the vertical spacing between the sensors, and δt is the time sampling. The uncertainty on the temperature sensors is 0.15°C.

observations of an internal tide beam were made on the northern part of the BoB (New, 1988; Pingree & New, 1989). Later, the theoretical work of Gerkema (2001) showed that the scattering of an internal tide beam is able to generate the NLIW observed offshore from the shelf break. Other generation sites for NLIW have been highlighted in the BoB such as the western end of the North Iberian slope (Azevedo et al., 2006). Despite the intense internal wave activity, no studies have focused on NLIW on the continental shelf.

2.2. Data Set

The ETOILE campaign (Lazure & Puillat, 2017) has been designed to study internal wave dynamics on the Aquitaine shelf. The study area was chosen for its straight coastline and simple bathymetry, which it was hoped would support simple cross-shelf internal wave propagation (Jackson et al., 2012). The observations presented here are from two moorings and a towed moving vessel profiler (MVP; Table 1). The moorings recorded temperature, pressure, and currents and were deployed from 9/07/2017 to 2/08/2017. The outer-shelf mooring (2L) was positioned close to the 150 m isobath and the inner-shelf mooring close to the 60 m isobath (Figure 1a). The 2L and 2C moorings had, respectively, 9 and 6 thermistors distributed between 70 cm above the bottom and 20 m below the surface, with a sampling period of 1 min (Table 1). Two bottom-mounted ADCP (RDI Sentinel 300 kHz) were deployed with a sampling period of 2 s (Table 1). The ADCP and thermistor string were collocated at the inner-shelf site but separated by 1.4 km at the outer-shelf (Table 1). Vertical profiles of conductivity, temperature, and depth (CTD) were performed during 25–29/07 2017, using an unpumped AML Oceanographic Micro CTD Sensor mounted on an MVP. The CTD sampled at 25 Hz, and the response times of the conductivity and temperature sensors were 25 and 100 ms, respectively. On 25–26/07, the MVP profiled along a 52-km long transect down to 300-m depth for the first two days at a boat speed of four knots. On 27–28/07, the MVP profiled down to a maximum of 100 m along a 15-km long transect at a boat speed of 6 knots. The MVP turned around 12 m above the bed for safety. In total, 8 transects were performed. The wind data come from the numerical model of METEO FRANCE AROME (0.025° horizontal resolution). The data set used in this study is taken at 44.0° latitude and −1.55° longitude, at 10 m above the surface.

2.3. Data Analysis

2.3.1. ADCP

The ADCP measurements were time-averaged over a 1-min window. We only kept the velocity measurements when all 4 beams passed quality checks. The first cell of each ADCP was at 4.5 mab (meters above the bottom). Because of sidelobe interference, we removed ADCP measurements within a distance from the surface corresponding to 1/10th of the total instrument depth, for both sites (7 m for 2C and 15 m for 2L). Due to the limited range of the ADCP, many values (at 1-s sampling) were missing at the 2L mooring from 15 to 50 m below the surface. u and v are the cross-shore (eastward when positive) and alongshore (northward when positive) velocity components, respectively.

To prepare the signals for filtering, we filled missing velocity values using a nearest neighbour interpolation. We flagged any such points and removed them from the final filtered records. We used the Demerliac tidal filter (Demerliac, 1974) to produce a subtidal temperature and velocity record. A description of the Demerliac tidal filter can be found in Simon (2007). This filter eliminates the tide, including its diurnal components, and resembles a low-pass filter with a 30-hr cutoff period. Tidally filtered velocity using the Demerliac filter (which uses hourly values) are referred to as background velocities in Section 3. A third order Butterworth band-pass filter was used to study tidal and high-frequency dynamics. We used a band-pass filtered baroclinic current between 4 and 15 hr in Section 3.2.2 to study the internal tide velocities.

The baroclinic current was computed as the total current minus the barotropic one. We computed the barotropic current by depth-averaging the velocity measurements from $H/10$ m below the surface down to 4.5 m above the bottom. For the barotropic current, we applied a band-pass filter between 4 and 15 hr after depth-averaging. In Section 4, we show 5-hr Butterworth low-pass filtered velocities to discuss the combined effect of tidal and subtidal currents on NLIW; we refer to this current as the fast-changing background current. To avoid any confusion, we explicitly cite the type of current we are studying in the text and in the figure captions.

2.3.2. Vertical Profile Transects

We converted the time series of the MVP profile to distance using the MVP speed and boat velocity. The MVP profiles were asymmetrical between the downward and upward casts. The downward cast was almost vertical due to the device free-falling at ∼6 m/s. The upward cast was slower, reaching a maximum vertical speed of 2.5 m/s. We interpolated the scattered MVP measurements onto a regular grid using the MATLAB interpolation package gridfit by D'Errico (2025).

2.3.3. From Temperature to Density Profile

We obtained a linear equation of state (Equation 1) from 3 days' MVP measurements between 2L and 2C (see green line Figure 1b).

$$\rho = -0.31\,T + 1031.19 \tag{1}$$

The use of a linear equation of state was a good first approximation since the correlation coefficient of the linear regression $r^2 = 0.99$ (see Figure A1). MVP measurements were carried out at the end of the campaign, and to check that this approximation was justified throughout the campaign, we used data from the global ocean eddy-resolving (1/12° horizontal resolution, 50 vertical levels, and daily output) reanalysis GLORYS model, between 2C and 2L over the entire campaign period, as we did not carry out continuous salinity measurements. The GLORYS data set revealed constant salinity ∼35.8 ± 0.2 for the whole month observation period from 20 m below the surface (see Figure A2). Therefore, for the whole month, we fit the density ρ to the mooring measured temperature T using Equation 1. We linearly interpolated the moored temperature observations (∼10 m apart) from moving pressure coordinates to a fixed vertical grid with 1-m resolution. We set a constant temperature from the highest sensor up to the surface using the measurement at the highest sensor (40 mab for 2C and 150 mab for 2L). Temperatures above the highest sensor are denoted "near-surface."

2.3.4. Background Stratification

We used the 24-hr low-pass filtered temperature field and use Equation 1 to compute the background density field at both moorings. We then computed the squared Brunt-Väisälä frequency N^2 with Equation 2.

$$N^2 = -\frac{g}{\rho_0}\frac{d\rho}{dz} \tag{2}$$

with ρ_0 the depth-averaged density evolving in time. Here the z-axis is positive upward. We imposed a constant temperature from the surface-most temperature sensor up to the surface to compute internal wave parameters. This corresponds to a completely mixed surface boundary layer with $N^2 = 0$ from the surface-most temperature sensor up to the surface.

2.4. Internal Tide Characterization

2.4.1. Phase Speed

We computed the modal structure $\phi(z)$ from the background stratification N^2 by solving the Sturm-Liouville problem

$$\frac{d^2\phi}{dz^2} + k^2 \frac{N^2 - \omega^2}{\omega^2 - f^2}\phi = 0 \tag{3}$$

with boundary conditions $\phi(\text{surface}) = \phi(\text{bottom}) = 0$ and the normalization condition $\max(\phi(z)) = 1$. k is the internal tide wave number. The solution assumes a flat bottom, and that the internal tide is a plane wave with a semidiurnal frequency ω. We computed the internal tide phase speed $c_{M2} = \omega/k$.

2.4.2. Internal Tide Amplitude

We computed the internal tide amplitude using a modal amplitude fitting method (Rayson et al., 2019). We recovered the amplitude of the three first modes A_n by least squares fitting the tidal buoyancy field (b_T) to its modal components (see Equation 4). The internal tide amplitude is taken as the mode-1 amplitude A_1:

$$b_T(z,t) = \sum_{n=1}^{3} A_n(t)\,\overline{N}^2(z)\phi(z) \tag{4}$$

The tidal buoyancy field is computed from the tidally filtered density field ρ_T as $b_T = -g\,\rho_T/\rho_0$. We computed ρ_T from the temperature field band-pass filtered around the semidiurnal frequency (4–15 hr), and we then added back the time-averaged temperature at each height (Figure 1b) to recover a stratified field. $\overline{N}^2$ is a double tangent function fitted on the time mean stratification profile. Here $\phi(z)$ was computed using the hydrostatic Taylor-Goldstein equation without the Coriolis term, which is a simplified version of Equation 3. Because the Coriolis parameter increases the propagation speed (eigenvalue) and does not affect the eigen vector, it can be neglected in the modal amplitude fitting. The modal amplitude fitting is often used on the raw density field, that is, the fast-evolving buoyancy field to compute the NLIW wave amplitude (Rayson et al., 2019). In Rayson et al. (2019) the internal tide amplitude is computed from a short-time harmonic analysis (STHF). Here, we verified the internal tide amplitude time evolution computed from both methods showed the same phase and similar amplitudes.

2.5. NLIW

2.5.1. Identification

We identified the NLIW from high-amplitude and high-frequency isotherms excursions. We computed the position and excursion of an isotherm by linear interpolation of the raw temperature field. We did this for all integer temperatures in the recording range (i.e., isotherms every 1°C). For NLIW identification, we applied an amplitude threshold to the 2-hr high-pass filtered excursions, denoted HF excursions (Section 2.5.1). We defined the polarity of the waves using the amplitude sign and confirmed the polarity of each wave with its vorticity using velocity measurements (Shroyer et al., 2009). NLIW of elevation/depression were propagating onshore so that the horizontal current under the waves crest was positive/negative for an x-axis positive toward the East. Therefore, we will refer to the vertical velocity pattern to describe the vorticity. An elevation wave has positive amplitude and negative vorticity, that is, a positive significant vertical velocity followed by a negative velocity in time. A depression wave corresponds to positive vorticity.

For an NLIW to be identified, we required the HF isotherm excursion to exceed a threshold value ($A_{\min}$) for more than 2 min. We defined a value for $A_{\min}$ based on the nonlinearity scaled by $\frac{A_{\min}}{H_s}$, where H_S is the vertical scale of the stratification (Helfrich & Melville, 2006). We define the vertical scale of the stratification as the height where the internal wave can propagate that is, where $N^2 > \omega^2$. It gives $N^2 > 1.4\,e^{-4}$ rad^{2}s^{-2}. In our case, the

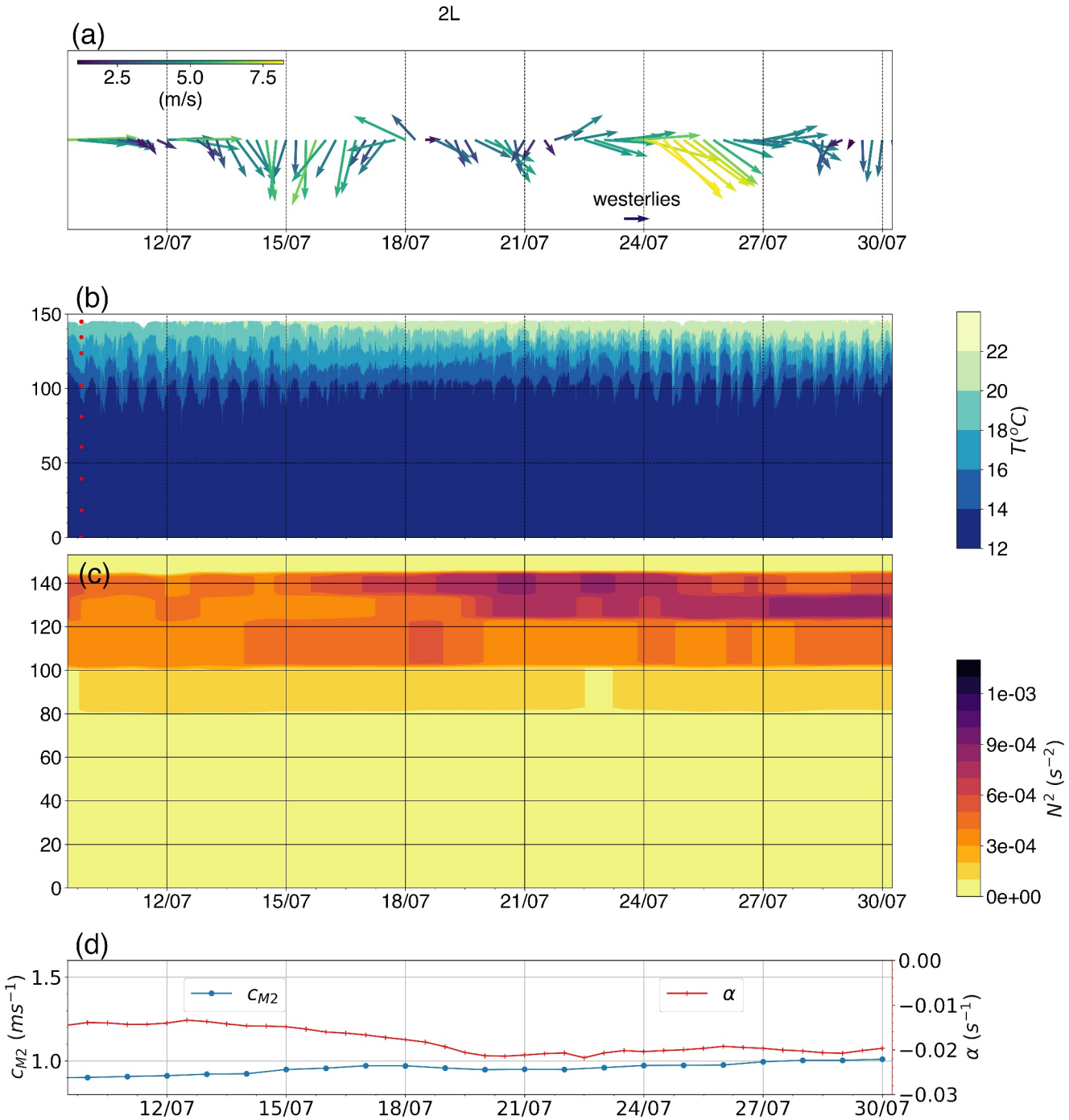

Figure 2. Background conditions observed at outer-shelf mooring 2L. (a) 24-hr low-pass filtered winds (quiver colors). (b) Temperature contours. Red dots indicate the position of the temperature sensors (Table 1). (c) Background stratification N^2. (d) Internal tide phase speed c_{M2} and the nonlinearity KdV coefficient α estimated from the background stratification.

stratification extended to 65 m below the surface in 2L (Figure 2c) and over the whole water column (62 m) in 2C (Figure 3e). To ease the computation, we set a constant value for both sites, $H_S = 65$ m. We chose an arbitrary nonlinearity ratio of 10% so that $A_{\min} = 0.1\ H_s$. We note the methodology does not allow one to identify NLIW smaller than 6.5 m. We chose this threshold as we were less interested in the dynamics of smaller waves and our sensor spacing did not permit detection of isotherm excursion below this.

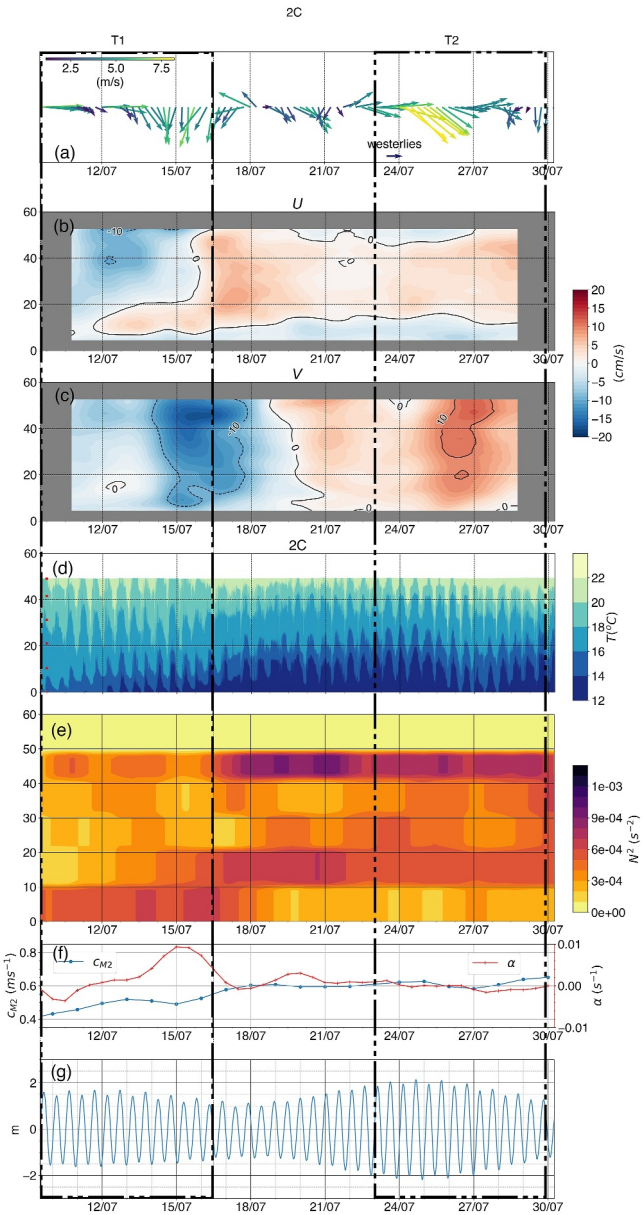

Figure 3. Background conditions observed at the inner-shelf mooring 2C. (a) 24-hr low-pass filtered winds in quiver colors. (b) Contours of background cross-shore currents U, black lines correspond to 0 and 10 cm/s currents; negative values are westward, and positive values are eastward. (c) Contours of background alongshore currents V, black lines correspond to 0, 10 cm/s currents; negative values are southward, and positive values are northward. (d) Temperature contours. Red dots indicate the position of the temperature sensors (Table 1). (e) Background stratification N^2. (f) Internal tide phase speed c_{M2} and the nonlinearity coefficient, α estimated from the background stratification. (g) Sea surface elevation.

At the outer shelf, we identified an NLIW event when at least three isotherms' HF excursion reached $A_{\min}$ (i.e., impacting at least a water layer with a 3°C temperature range). At the inner shelf, we identified waves of elevation when the 16°C isotherm HF excursion reached $A_{\min}$. We identified waves of depression when the 19°C isotherm HF excursion reached $A_{\min}$.

2.5.2. Characteristics

We measured the NLIW amplitude (at 2C and 2L) A as the maximum HF excursion reached by one of the three isotherms around 16°C ± 1°C for elevations and around 19°C ± 1°C for depressions. The NLIW timescale T was defined as the time difference between two minimum excursion of the HF isotherm used to compute A. The wavelength λ was computed and corrected for any Doppler shift effect due to barotropic current as $\lambda = T\cdot(c_{nl} + \overline{u})$, where c_{nl} is the propagation speed and $\overline{u}$ the cross-shore depth-averaged current. The NLIW steepness, s, was measured as $s = A/\lambda$.

We used different methods to compute c_{nl} at the outer shelf and the inner shelf. At the inner shelf, the moorings were collocated; therefore, we measured c_{nl} and the direction of each NLIW from the phase-lagged backscatter method developed by Scotti et al. (2005). We measured enhanced ADCP backscatter close to the surface for depression waves and close to the bottom for elevation waves. Therefore, we used different ADCP bins to apply the method. We used ADCP bins between 5 and 22 mab for the elevation waves and between 40 and 49 mab for the depression waves. Only events with well-correlated backscatter signatures between the four beams were considered (more than 60% over the time window interval considered). We quantified the error induced by the arbitrary choice of window length by using four different time windows (windows between 11 and 9 min). We only retained the propagation speed when the spread in estimates was small, that is, less than 0.1 m/s and less than 45° for the angle, for a minimum of 3 values. The final c_{nl} and the angle presented below are the mean values. The maximum uncertainties we obtained were 0.06 m/s for the propagation speed and 32° for the angle. Not all NLIW had a defined backscatter signature and not all estimates had tolerable uncertainty; therefore, not all waves have an estimate for c_{nl}. For the outer shelf, we used the time lag between the maximum isotherm excursion and the zero-crossing of the vertical velocity as the moored temperature measurements and the ADCP velocity measurement were aligned in the direction of wave propagation (east/west Table 1, derived by MVP measurement) and separated by 1.4 km (P0 in Table 2). At the outer shelf, only the waves tracked by the MVP were characterized. The propagation speeds measured with both methods were corrected for any Doppler shift effect due to barotropic current.

2.5.3. KdV Environmental Parameters

We analyzed the effect of background stratification and shear using the simple Korteweg-De Vries equation with and without background shear with velocity profile U:

$$\frac{\partial \eta}{\partial t} + c_0\frac{\partial \eta}{\partial x} + \alpha\eta\frac{\partial \eta}{\partial x} + \beta\frac{\partial^3 \eta}{\partial x^3} = 0 \quad (5)$$

Here, α and β are the quadratic nonlinear and dispersive coefficients, respectively. We computed alpha without and with (subscript s) shear

Table 2
Propagation Speed Within the Wave Packet at Different Locations Across the Shelf

Position n°	H (m)	Distance from the shore (km)	Time (HH:MM)	c_{nl} (m/s)	Method	Wave polarity
P0 (Figures 7d and 7e)	150	49	07:00	0.96	Lag between velocity and temperature	Depression
P1 (Figure 7a)	75	12	20:11	0.78	Lag from P0 to P1	Depression
P2 (Figures 7f and 7g)	62	9	22:15	0.61 ± 0.05	Lag backscatter method see Section 2.5.2	Mixed polarity
P3 (Figure 7b)	53	7	23:21	0.5	Lag from P2 to P3	Elevation
P4 (Figure 7c)	49	5.5	00:28	0.4	Lag from P3 to P4	Elevation

Note. At the MVP positions, the propagation speed corresponds to the time lag appearance of the wave packet between the MVP and mooring measurements, and the barotropic current was removed. At the mooring site, the propagation speed was computed from backscatter measurements as described in Section 2.5.2.

$$\alpha = \frac{3}{2} c_0 \frac{\int_{-H}^{0} \phi' dz}{\int_{-H}^{0} \phi'^2 dz} (\mathrm{s}^{-1}) \tag{6}$$

$$\alpha_s = \frac{3}{2} \frac{\int_{-H}^{0} (c_0 - U)\, \phi'^3 dz}{\int_{-H}^{0} (c_0 - U) \phi'^2 dz} (\mathrm{s}^{-1}) \tag{7}$$

where

$$\phi' = \frac{d\phi}{dz}$$

The modal structure function ϕ and the linear propagation speed c_0 are determined from the Taylor-Goldstein equation with shear (Equation 8) and without shear (Equation 9), using the usual hypothesis of high-frequency ω, long wave-limit, and under the Boussinesq and rigid lid approximation (Grimshaw et al., 2004; Rayson et al., 2019; Shroyer et al., 2011). The NLIW propagate approximately in the cross-shore direction (see Section.4 below); therefore, we only considered the cross-shore background component U(z) in the following equation with shear:

$$\frac{d}{dz}\left[(c_0 - U)^2 \frac{d\phi}{dz}\right] + N^2(z)\, \phi = 0 \tag{8}$$

$$c_0 \frac{d^2\phi}{dz^2} + N^2(z)\, \phi = 0 \tag{9}$$

Boundary conditions for both problems are $\phi(z = \text{surface}) = \phi(z = \text{bottom}) = 0$. Moreover Grisouard and Staquet (2010) show a negligible effect of the Coriolis parameter for waves of approximately half an hour or less period. We verified this condition for all the NLIW studied here. When considering the shear effect, we interpolated the background velocity to the surface and the seabed using the nearest neighbor. To solve Equation 8, we used the shooting method described in detail in Rayson et al. (2019). Note that the numerical computation does not converge when $|U| > c$ for all depths or for sharp changes of U with z. Here, we only compute the α parameter.

3. Observations of Tidal and Subtidal Processes

Here, we focus on the subtidal and internal tide conditions at the inner- and outer-shelf locations to provide context to the variability in the NLIW. We use α to characterize the likely impact of the background stratification conditions on the NLIW field.

3.1. Outer Shelf

At the outer shelf, the surface pycnocline strengthened over time as the near-surface temperature increased (Figures 2b and 2c). The stratifications varied very little under moderate northerly winds from 13/07–17/07 and

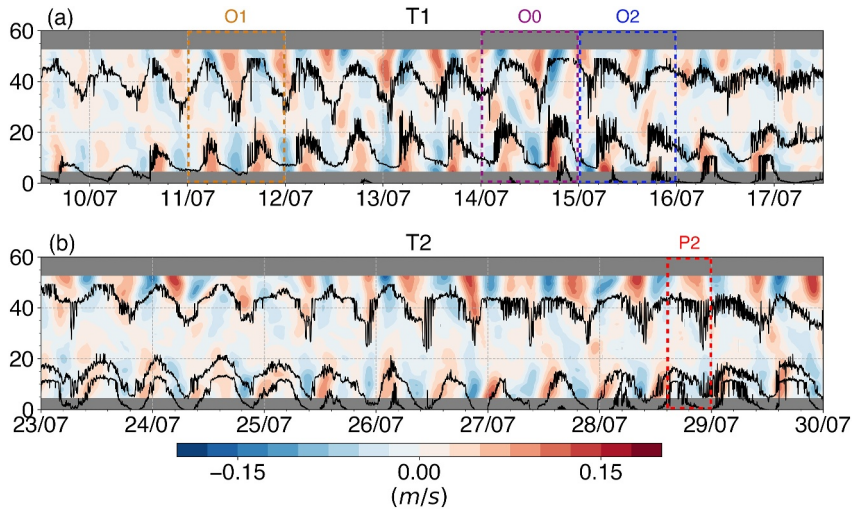

Figure 4. Observations at the inner-shelf 2C mooring of the cross-shore baroclinic current band-pass filtered between 4 and 15 hr (colors) and isotherms (black lines) for the two periods of interest defined in Section 3.2.1 (See black rectangles in Figure 3.). (a) The dominant near-bed pycnocline period T1 with the 19°C, 16°C, and 13°C raw isotherms (black lines). (b) The dominant near-surface pycnocline period T2 with the 19°C, 14°C, and 13°C isotherms (black lines).

strengthened from 18/07 under initially weaker winds (Figures 2a and 2c). The wind-driven circulation did not seem to impact the background stratification appreciably. At the outer shelf, the α was negative for the entire observation period, indicating waves of depression would likely be the predominant response (red curve in Figure 2d).

The internal tide was predominantly mode-1 with a clear spring-neap variation in amplitude (Figure 2b) and was phase-locked with the barotropic tide (not shown). The vertical mode-1 amplitude never exceeded 0.1 H, with a maximum of 15 m during spring tides and minimum of 5 m during neap tides (not shown). The mode-1 internal tide phase speed increased by 10% between the first and second spring tide (blue curve Figure 2d) in response to changing background conditions. These first and second spring tide periods are herein referred to as periods T1 and T2, respectively.

3.2. Inner Shelf

3.2.1. Subtidal Dynamics

The stratification and the internal tide were more responsive to subtidal wind-driven dynamics at the inner-shelf site, as compared to the outer shelf. Northerly winds (14/07 to 16/07 Figure 3a) corresponded with an alongshore, southward depth-averaged current (Figure 3c), an offshore current close to the surface and onshore in the interior (Figure 3b), and a decrease of the near-bed temperature and an outcrop of the near surface isotherms (Figure 3d). This is characteristic of an upwelling event during strong near-bed stratification conditions (e.g., Lentz & Chapman, 2004). After 16/07, a near-bed layer of cold water developed (Figure 3d). A few days after the strong westerly winds (27/07 Figure 3a) the near-bed cold water disappeared (Figure 3d) as the northward barotropic current increased (Figure 4c), similar to weak remotely generated downwelling events previously studied on the Aquitaine shelf (Batifoulier et al., 2012; Kersalé et al., 2016).

At the beginning of the record (period T1), there was a double pycnocline, coincident with a vertically sheared cross-shore background current (Figure 3e). We estimated that the near-bed pycnocline was 30% stronger on average than the near-surface pycnocline in this period, but note that the vertical resolution of our temperature sensors (see Figure 1d) did not permit a precise description of the pycnocline position and width. The estimated nonlinearity coefficient, α, changed from negative (waves of depression) to strongly positive (waves of elevation) during this period as the near-bottom cold-water influx strengthened the bottom pycnocline (Figure 3f). During T1, c_{M2} increased from 0.4 to 0.6 m/s, solely due to the strengthening of the bottom pycnocline (Figure 3f). We would expect the observed background shear to also modify the internal tide propagation, and we return to this in

the next section. At the beginning of T1 (on 9/07), there was already a double pycnocline. Upwelling amplified the double pycnocline by reducing the surface pycnocline and reinforcing the bottom pycnocline.

During the second spring tide period (period T2), the bottom pycnocline was located further from the seabed and the surface pycnocline strengthened and became dominant (Figure 3e). The indicative NLIW parameters were relatively constant for this period with α close to 0 and $c_{M2} \sim 0.6$ m/s (Figure 3f).

3.2.2. Internal Tide and Semidiurnal Tidal Bores

At the inner-shelf site, the internal tide was again dominated by a mode-1 wave (not shown) with maximum amplitude ~20 m. The maximum *A/H* ratio was 3 times higher than at the outer shelf, leading to a steepened internal tide. The spring-neap variation in amplitude was less distinct than on the outer shelf (Figure 3d), but there was a marked subtidal influence.

During period T1 (near-bed pycnocline and shear in the subtidal cross-shelf velocity), we observed cold semi-diurnal bores with steep fronts associated with packets of NLIW of elevation (Figure 4a). The back face of the bore was characterized by a slower return to warmer water as the near-bed baroclinic current turned onshore (Figure 4a). These bore dynamics were similar to those observed at other sites around the world (Cheriton, McPhee-Shaw, Storlazzi, et al., 2014; Jones et al., 2020; Masunaga et al., 2019; McSweeney et al., 2020), which have been described as canonical bores. Canonical bores form on gentle slopes and result in a strong temperature front (Walter et al., 2012). We will focus on the NLIW variability in Section 4. During T1, both the near-surface and near-bed internal tide currents were stronger (up to three times) than the barotropic current (Figure 4a and ellipses in Figure 1d).

During period T2, when there was a dominant surface pycnocline, we predominantly observed a steepened internal tide with NLIW at the upper pycnocline (19°C isotherm in Figure 4b). The near-bed internal tide oscillations were smaller in amplitude and more symmetrical than those observed during T1, with near-bed currents of similar magnitude to the barotropic tide (Figure 4b). The near-surface internal tide currents were stronger, regularly reaching 0.15 m/s (3 times the measured barotropic current).

4. NLIW Observations

In this section, we describe the NLIW at both the inner- and outer-shelf sites. In Section 4.1, we provide summary statistics of the identified NLIW and investigate the influence of the background stratification and shear on the NLIW field. We show that changes in the background conditions (Section 3.2) greatly alter the NLIW response. In Sections 4.2 and 4.3, we examine individual wave packets passing the inshore site, focusing only on packets containing waves of elevation (i.e., We do not elaborate on packets of depression that propagate inshore.). Section 4.2 is devoted to the well-studied case of depression waves changing polarity (termed mixed polarity) in shallower water when the near-surface pycnocline is dominant. The packets of coexisting elevation and depression waves (termed opposite polarity) observed under the near-bed dominant pycnocline are presented in Section 4.3. The analysis suggests very different evolution mechanisms between the first T1 (near-bed dominant pycnocline and subtidal current shear at the inner shelf) and second T2 (near-surface dominant pycnocline period at the inner shelf) spring tides. The results have implications for the longevity of the wave packets and the nature of interaction between waves of depression and elevation within the wave packets.

4.1. Summary Statistics

At the outer shelf, 56 NLIW of depression were identified for the whole period. Most of the NLIW coincided with larger internal tide amplitude, and the majority occurred during the second spring tide period (Figure 5b) and just before low internal tide. No elevation waves were observed as anticipated by the negative α (Figure 5a). The background shear did not impact α substantially at this site (circles Figure 5a). Previous observations in the central part of the BoB reported waves around 50–60 m that propagated at speeds of approximately 1 m/s (New & Pingree, 1992).

At the inner shelf, 46 elevation and 48 depression waves were observed (94 total). The vast majority of depression waves occurred during the ebb just before the low internal tide. The NLIW had distinct features depending on their polarity. Typically, the elevation waves were steeper (median $s \sim 10^{-2}$) and slower (median $c_{nl} \sim 0.27$ m/s)

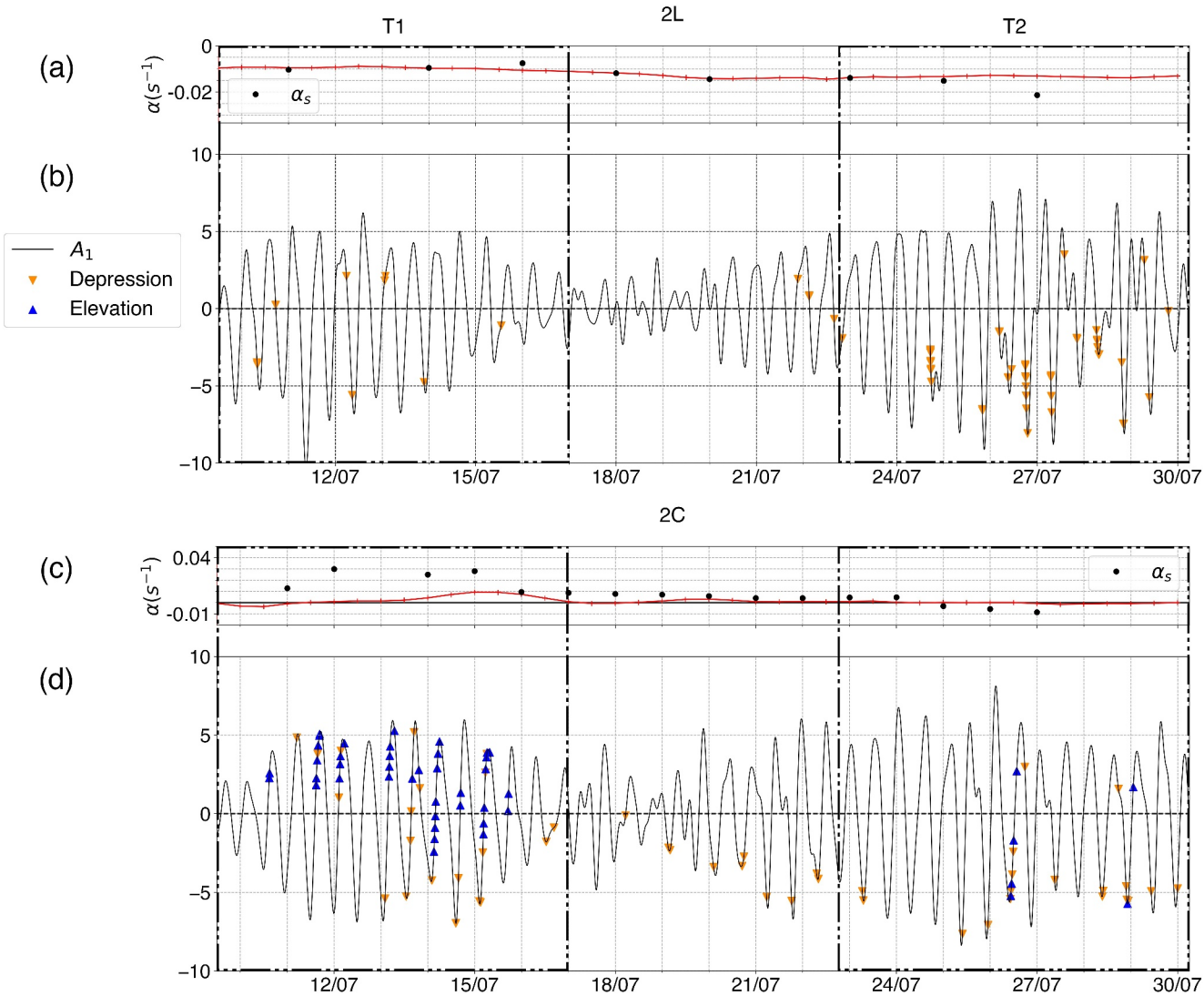

Figure 5. (a, b) Measurements at the 2L outer-shelf mooring. (c, d) Measurements at the 2C inner mooring. (a, c) KdV nonlinear coefficient evolution due to subtidal changes with no shear (red line) and with shear α_s (black dots). (b, d) Mode-1 internal tide amplitude (black line). Time of maximum displacement of NLIW of elevation (dark blue upward triangles) and depression (light orange triangles).

than wider (median $s \sim 10^{-3}$) and faster depression waves (median $c_{nl} \sim 0.42$ m/s) (Figures 6c and 6d). Both polarities of NLIW had a wide distribution of amplitude, with a maximum value of 25 m (Figure 6a). Note that we could only estimate the propagation speed c_{nl} and geometrical parameters for 27 elevation waves (out of 46) and 18 depression waves (out of 48) (see Section 2.5.2).

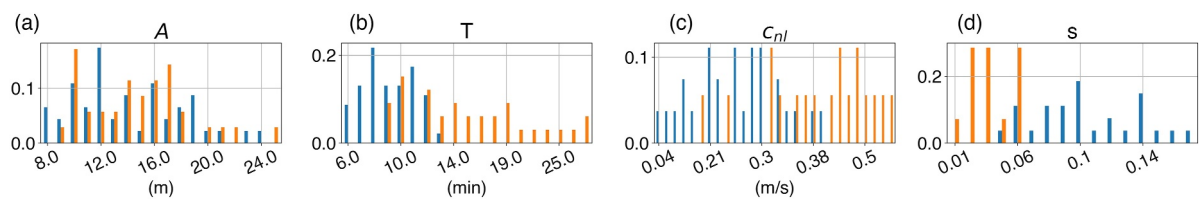

Figure 6. Histograms of the NLIW characteristics on the inner shelf normalized by the number of available measurements for a given polarity. Blue values are for elevation waves, and orange for depression waves. (a) A(m) is the wave amplitude; (b) T(min) is the timescale; (c) c_{nl} is the propagation speed, and (d) s is the wave steepness. NLIW characteristics are defined in Section 2.5.2. We computed the geometrical parameters of 48 depression and 46 elevation waves. We computed propagation speed and steepness for 18 depression and 27 elevation waves (Section 2.5.2).

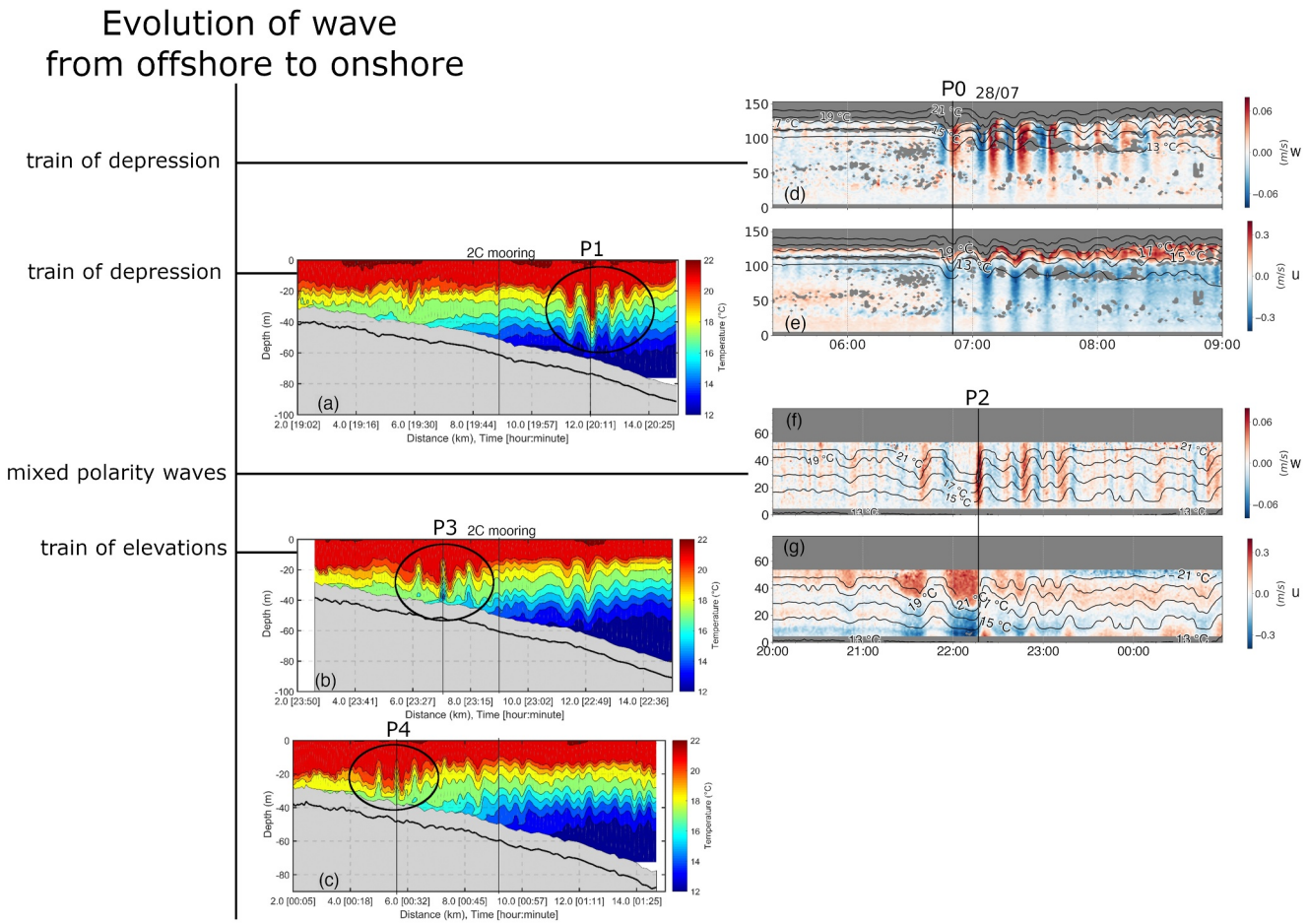

Figure 7. Onshore propagation of a packet of NLIW from offshore (top) to onshore (bottom) using moored and moving vessel profiler (MVP) observations between 28/07 and 29/07 (a–c) Fraction of the MVP transect (location shown in Figure 1) measurements of the temperature field showing the propagation of a packet of NLIW. Black lines correspond to the isotherms at 1°C intervals. The bold dark line shows the seabed. P0, P1, P2, and P4 correspond to the positions in Table (2). (d, e) Outer-shelf 2L moorings measurements: (d) vertical velocity w in 2L and (e) baroclinic cross-shore current u. (f, g) Inner-shelf 2C moorings measurements: (f) vertical velocity w and (g) baroclinic cross-shore current u.

Depression waves were present at the inner-shelf site during both spring and neap tide and even when the local value of α was positive (Figures 5c and 5d). The presence of elevation waves was strongly influenced by subtidal conditions. Elevation waves were much more prevalent during T1 than T2 (Figure 5d). During spring tide T1 (near-bed dominant pycnocline and subtidal current shear at the inner shelf), the background shear heavily influenced the value of α, increasing it by a factor of 4 compared to the shear-free formulation (circles in Figure 5c). Under these conditions, we observed packets of elevation waves during most tidal cycles. We note that the salinity change near the surface would be expected to impact the value of α.

4.2. Nature of Inner-Shelf NLIW of Elevation During the Near-Surface Dominant Pycnocline Period (T2)

On two occasions (26/07 and 28/07, Figure 5b), the NLIW of depression observed at the offshore mooring had transitioned to NLIW of mixed polarity by the time they passed the inshore mooring. We focus on the group that passed the inshore mooring on the 28th (Figures 7f and 7g), as the MVP captured this wave on three occasions: once between the moorings and twice inshore of the inner-shelf mooring (Figures 7a–7c).

At the offshore mooring, the waves of depression were symmetrical, displaced the thermocline by ∼20 m, and were rank-ordered (Figures 7d and 7e). No other waves were observed around this time at the offshore mooring (Figure 5b). Thirty-seven kilometers inshore, these waves were observed 13 hr later and had slowed down (propagation speed from ∼1 to 0.78 m/s between P0 and P1 Table 2); the waves were no longer rank-

ordered, and the first two waves had a steeper back face than the front face (Figure 7a). By the time the waves reached the inner-shelf mooring, where $\alpha \sim 0$, they at 06:15, were of mixed polarity (Figures 7f and 7g). No other waves were observed around this time at the onshore mooring (Figure 5d). The depression waves in the packet were asymmetrical with a broad front face, a weak downward velocity, and a steep rear face coinciding with a sharp upward motion (Figure 7g). These waves of depression had similar characteristics to the waves undergoing polarity reversal on the New Jersey coast (Shroyer et al., 2009). Between the high-amplitude depression waves, we observed small amplitude elevation waves (between 22:15 and 23:15) with enhanced near-bed onshore horizontal velocity (see after P2 Figure 7g). Both depression and elevation waves perturbed the isotherms throughout the entire water column (Figures 7f and 7g). Once the wave packet passed the inner-shelf mooring, it evolved into three waves of elevation of ∼20 m amplitude (Figures 7b and 7c).

The combination of moored data and MVP profiles clearly indicates that the mixed polarity packets we observed at the inner-shelf site during T2 were transitioning from waves of depression to elevation.

4.3. Nature of Inner-Shelf NLIW of Elevation During the Near-Bed Dominant Pycnocline Period (T1)

During period T1, under double pycnocline conditions and a fast-changing background current (here a fast-changing background current refers to 5-hr low-pass currents, see Section 2.3.1), the nature of NLIW was much more varied. We identified four distinct types of NLIW packets on semidiurnal bores. We used the internal Iribarren number, for example, the ratio of the bottom slope with the square root of the offshore internal tide slope to classify the bores observed at the study site. The internal Iribarren number was estimated to be around 0.15 using the bottom slope between 2L and 2C, the maximum amplitude of the internal tide and the associated propagation speed at 2L, which are given in the previous section. A small internal Iribarren number is associated with canonical bores (Walter et al., 2012).

4.3.1. Packets of Elevation Waves on a Semidiurnal Bore

During spring tide conditions coincident with a double pycnocline, for example, on 14/07 (denoted O0 in Figure 4), depression and elevation NLIW were both observed, but at distinctly different phases of the internal tide (Figure 8a). Packets of high-amplitude elevation waves arrived at the front face of bores every 12 hr (Figure 8a), with propagation speeds (median ∼0.28 m/s) (blue triangles Figure 8c) approximately half the value of the internal tide phase speed c_{M2} (∼0.5 m/s) (Figure 2d). Depression waves preceded the bores and occurred at low internal tide (when the 19°C reached its maximum depth). They propagated twice as fast as the elevation waves (similar speed to c_{M2}) (orange triangles Figure 8c).

On 14/07, we observed two successive packets of elevation NLIW (03:00 and 18:00 Figure 8). The two successive packets of elevation waves had appreciably different characteristics. Past studies have revealed that the local velocity and stratification preceding the packets lead to NLIW variability (Davis et al., 2020; Masunaga et al., 2016; McSweeney et al., 2020). The bottom temperature decreased for the 6 hr following the elevation wave packet (Figure 8e). Similar observations of cold water propagating upslope with coincident boluses were described by Davis et al. (2020).

Wave packets of simple elevation waves (Figure 9) were identified by the near-bottom isotherms rising upward; almost no modification of the near-surface isotherms was observed. At the same time, we observed enhanced positive horizontal velocity near the bed (Figure 9a) and enhanced vertical velocities, which reached more than 10 cm/s (Figure 9b). The horizontal velocity under the wave crests was around 0.25 m/s (Figure 9a), which was 5 times the cross-shore barotropic current magnitude. The two leading waves were small (less than 6 m) and followed by a high ($A = 24$ m) and steep (∼0.2) wave, associated with a transient drop of 0.5°C of the bottom temperature (Figure 9c) at 16:40. Within the wave, a core with well-mixed water (temperature differences did not exceed 0.5°C within the core in Figure 9) was up to 15 m high. Consequently, the 15°C, 16°C, and 17°C isotherms were strained and increased the stratification around the 20–30 mab region as expected in a bolus (Ghassemi et al., 2022). The combination of bolus-like waves and elevation waves was regularly observed. No signs of depression waves were observed in the wave train.

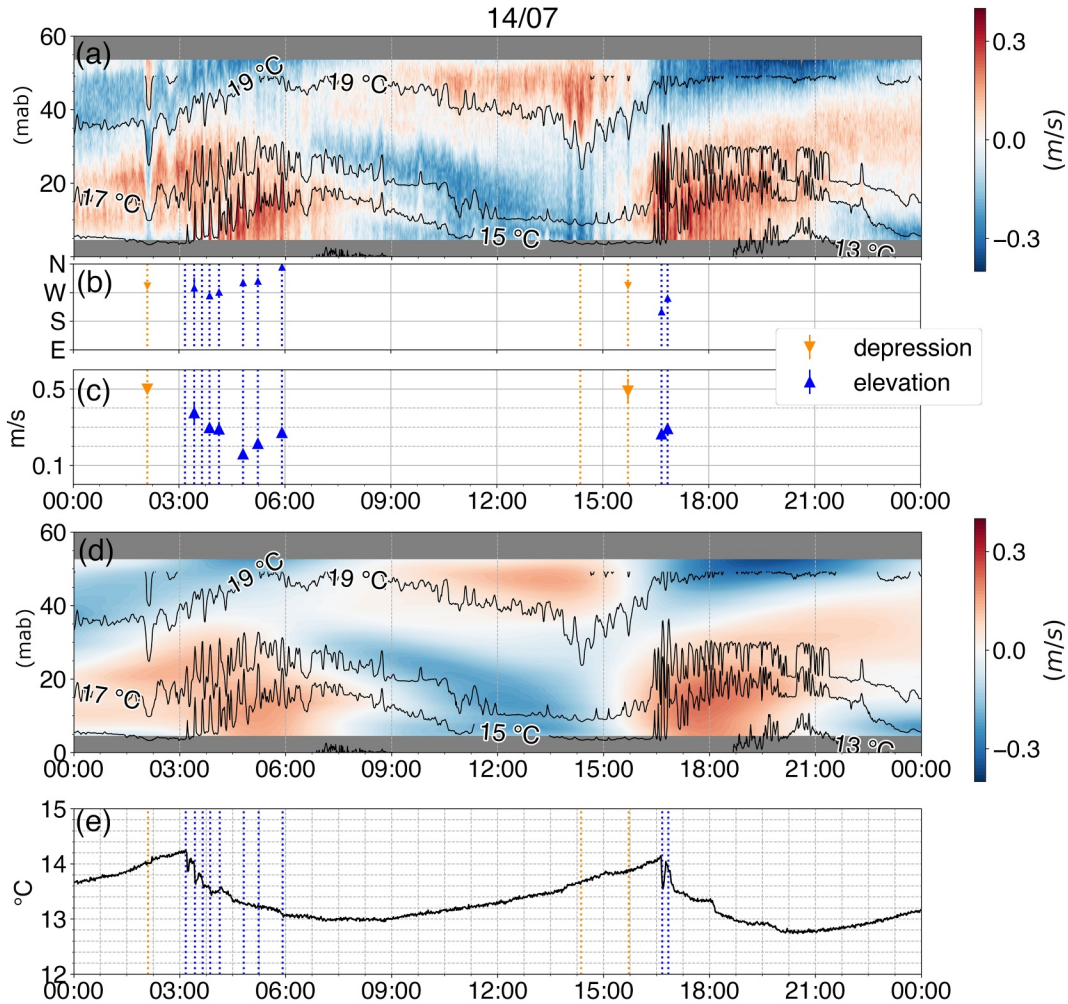

Figure 8. (a) Cross-shore total velocity. (b) Direction of arrival of the NLIW (Blue triangles correspond to the elevation waves, and orange triangles correspond to the depression waves). The dotted line corresponds to the time when an NLIW was observed (orange lines correspond to depressions, and blue lines to elevations). (c) NLIW propagation speed (Blue triangles correspond to the elevation, and orange triangles correspond to the depression.). (d) Fast-changing background current (5 hr low-pass filtered) cross-shore velocity. Note that here cross-shore velocity includes the tidal and subtidal baroclinic currents whereas the velocity in Figure 4 was band-pass filtered, and the depth-averaged current was removed. (e) Bottom temperature 70 cm above the seabed (black line).

4.3.2. Packets of NLIW of Opposite Polarity on a Semidiurnal Bore

During the first tidal cycles coincident with the near-bed dominant pycnocline (denoted O1 in Figure 4), we observed two packets of elevation waves (defined here as a grouping over 2 hr or less) that had depression waves propagating within them (Figure 10). Within both packets, small elevation waves (less than 12 m) propagated on the lower pycnocline, and one large depression wave (~17 m) propagated on the upper pycnocline (15:00 and 03:00 in Figure 10a). Within the second packet, elevation and depression waves were traveling at a similar speed (0.38 m/s) and similar direction. Unfortunately, our method did not allow us to estimate the propagation speed of the first wave of depression.

The bottom temperature was oscillating at the semidiurnal frequency and decreased by 0.8°C between the two tidal cycles (Figure 10e). The bottom temperature also sharply decreased at the timescale of the NLIW (Figure 10e), similar to the elevation wave packets on the semidiurnal bore (Section 4.3.1). For both packets, the first wave was likely to be a bolus, associated with a sharp, but transient drop in temperature (Figure 10e). Bolus-like waves were coincident with a 0.8°C temperature drop near the bed (Figure 11c).

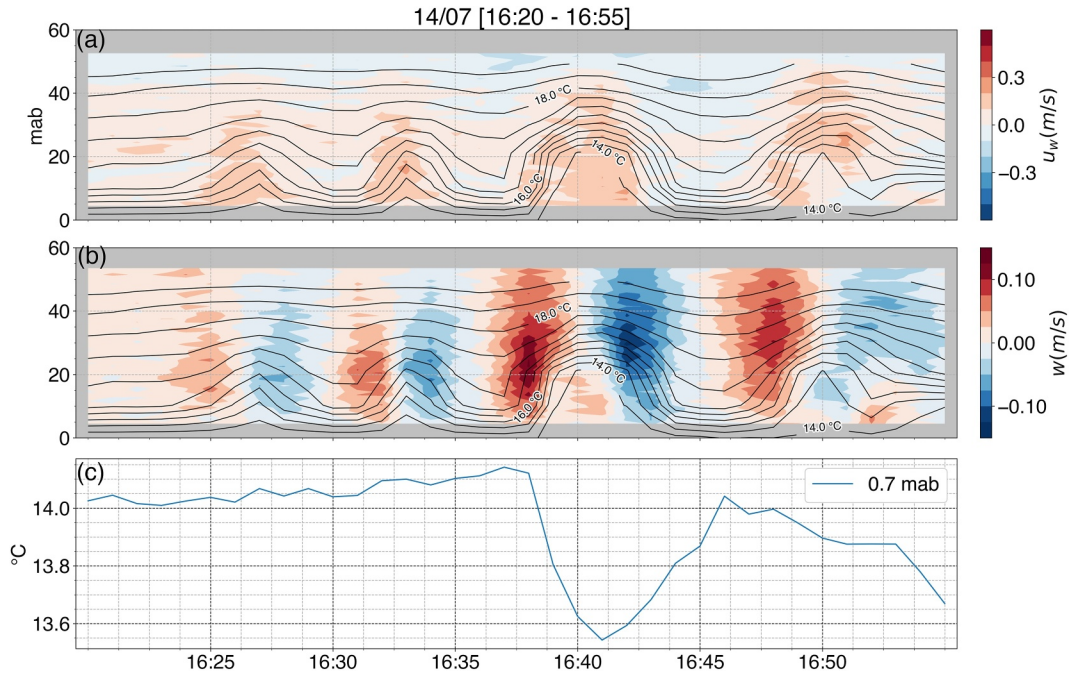

Figure 9. Leading NLIW from the wave train on 14/07. Black lines show isotherms every 0.5°C. (a) Horizontal residual velocity between the total velocity and the fast-changing background velocity, in the mean direction of the wave propagation u_w (color). (b) Vertical velocity w (color). (c) Bottom temperature 70 cm above the sea floor.

On both tidal bores (Figure 10), the NLIW were a combination of depression waves and elevation waves (shown for first packet in Figure 11). When we observed depression/elevation waves, the horizontal velocity under the waves was enhanced negatively/positively near the seabed (Figure 11a). At the same time, the vertical velocity increased. For elevation waves, we measured a positive vertical velocity followed by a negative vertical velocity (16:30 Figure 11b). For a depression wave, we first measured a negative vertical velocity followed by a positive vertical velocity up to 10 cm/s (15:35 Figure 11b). Only the first elevation wave was a bolus by our definition of a strong decrease in bottom temperature in the core (14:47 Figure 11c). The following elevation waves were not classified as boluses as the decrease in temperature within the wave core was smaller than the bottom temperature after its passage (14.3°C under the third elevation wave 15:25 and 14.5°C at 15:40 (Figure 11)). At the end of the train, the bottom temperature increased from 14°C to 14.6°C for less than 10 min, between the last two elevation waves, and decreased down to 14°C after the last elevation wave. The transient increase of bottom temperature was because of the downward displacement of the isopycnals (Figure 11c). As in the previous section, the elevation wave packet was a combination of bolus-like waves and simple elevations waves (Section 4.3.1). In this case, a depression wave surrounded by elevation waves was observed.

The horizontal velocity within the depression wave was difficult to interpret. When the depression wave was measured, around 15:35, the horizontal velocity was close to 0 (Figure 11a). Within the depression wave core, we would expect a positive value of the horizontal velocity. We may not observe the correct velocity field associated with the depression wave because the depression wave did not propagate in exactly the same direction as the elevation waves. Another possible reason why we did not observe positive horizontal velocity near the surface is the impact of ADCP beam spreading, which could have averaged over different parts of the wave core, reducing the velocity to zero. Near the surface, 45 m above the ADCP, the beams are separated by 33 m. The vertical velocity changes signs in around 5 min, and the wave should propagate around 0.5 m/s (We use an average value because we could not measure the propagation speed in this specific situation.), which gives a wavelength of 150 m. Only three points in time are measured within this depression wave, which may be too scarce for the ADCP to correctly measure the horizontal velocity.

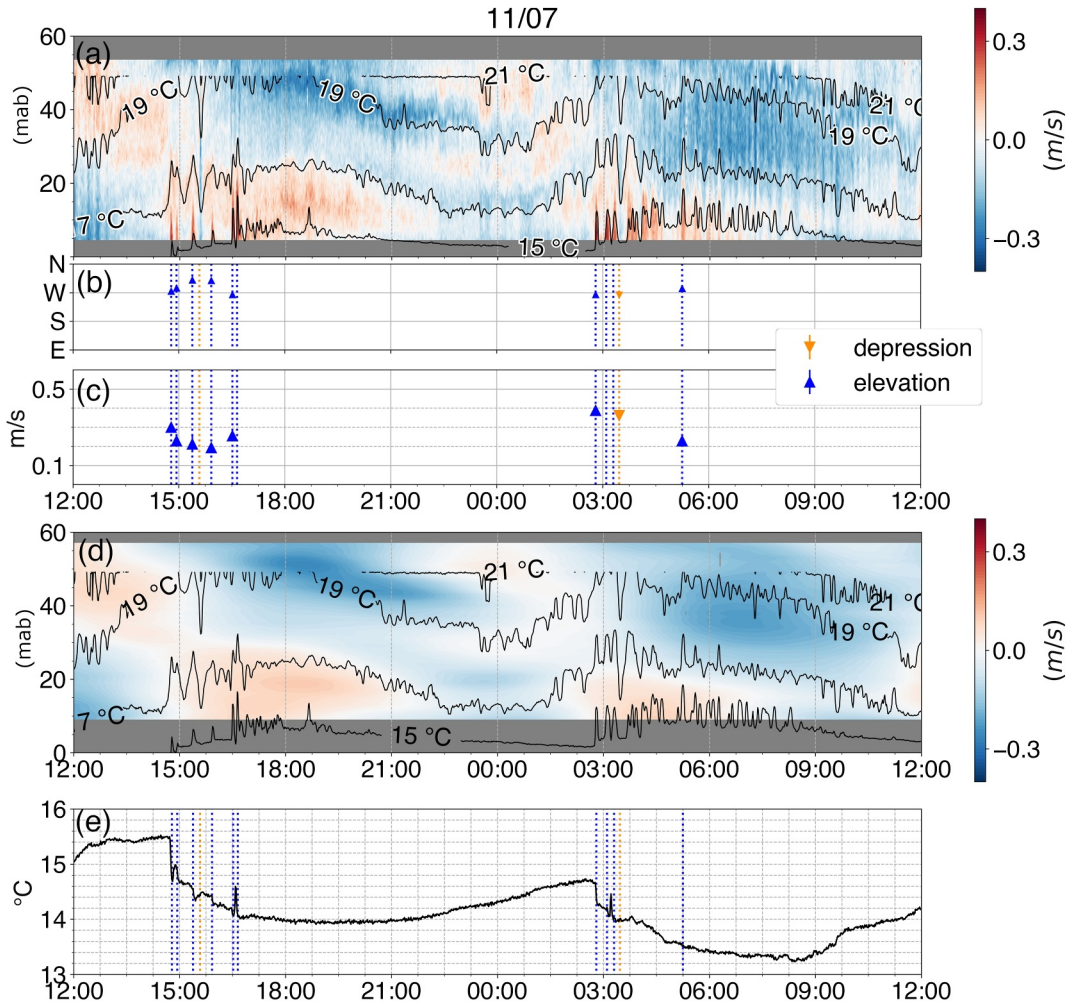

Figure 10. (a) Cross-shore total velocity. (b) Direction of arrival of the NLIW (Blue triangles correspond to the elevation waves, and orange triangles correspond to the depression waves). The dotted lines correspond to the times when an NLIW was observed (orange lines correspond to depressions, and blue lines to elevations). (c) NLIW propagation speed (Blue triangles correspond to the elevation, and orange triangles correspond to the depression). (d) Fast-changing background current (5-hr-low-pass filtered) cross-shore velocity. Note that here the cross-shore velocity includes the tidal and subtidal baroclinic currents whereas the velocity in Figure 4 was band-pass filtered and the depth-averaged current was removed. (e) Bottom temperature 70 cm above the seabed (black line).

4.3.3. Packet of NLIW of Opposite Polarity Superposed

As the bottom stratification increased, we observed elevation waves up to 23 m within a train of NLIW depression waves around 18 m in height (Figure 12). The opposite polarity packet was observed only on the first tidal cycle on 15/07 and did not repeat on the following one (Figure 12, denoted O2 in Figure 4). The fast-changing background current had mode-1 vertical structure prior to the first bore and had a higher order vertical structure with an increased number of velocity inversion points prior to the second bore from 9:00 to 16:00 (Figure 12d).

The tidal bore on the 15/07 started with a series of high-amplitude boluses (Figure 13 left) and ended with NLIW of depression among ordinary elevation waves (Figure 13 right). The leading boluses were rank-ordered in amplitude (Figure 13 left) and led the cold water bore arrival (Figure 12e). At the beginning of the packet, the bottom temperature decreased within the boluses and increased between the boluses. The NLIW at the end of the packet were coincident with a constant bottom temperature 0.6°C lower than the bolus cores (Figure 13f). During the bolus' propagation, no signs of depression waves were observed, the temperature at 40 mab was constant, and

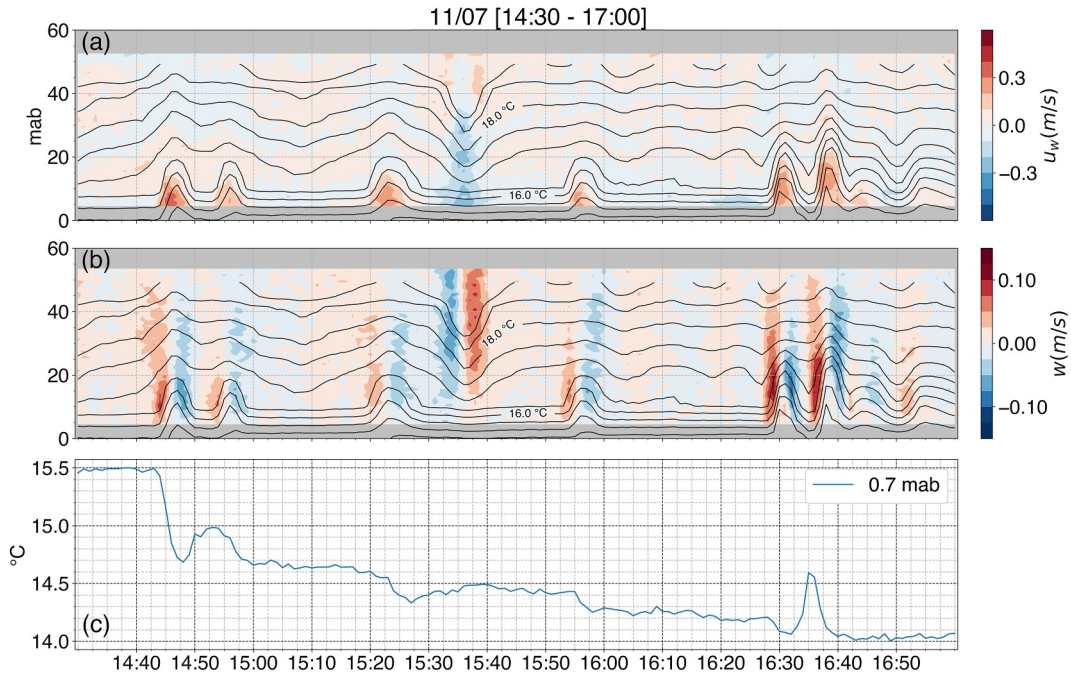

Figure 11. Focus on the NLIW train on 11/07 between 15:15 and 16:15. Black lines show isotherms every 0.5°C (black lines). (a) Horizontal residual velocity between the total cross-shore velocity and the fast-changing background cross-shore velocity in the mean direction of the wave propagation u_w (color). (b) Vertical velocity w (color). (c) Bottom temperature 70 cm above the sea floor.

the near-surface temperature 40 mab was constant (Figure 13 left). At 06:12 and 05:57, the near-surface temperature increased as depression waves passed at the end of the packet (Figure 13 right).

At the end of the packet, NLIW of depression were observed just before and after an elevation wave (05:55-06:20 Figure 13 right). The biggest vertical displacement depression wave was observed at 06:15 when the 19°C isotherm was displaced to 40 mab. At the same time, we measured a negative horizontal speed between 0.1 and 0.3 m/s, close to the seabed, and between 4 mab and 20 mab from 6:10 to 6:20 (Figure 13d). At 06:15, the vertical velocity reached a maximum of 5 cm/s at 40 mab within the depression wave (Figure 13e). The waves at the end of the packet had very different propagation speeds (Figure 12c). The elevation wave at 06:05 propagated at 0.35 m/s (Figure 12b); the following depression wave at 06:15 propagated at $c_{nl} \sim 0.55$ m/s, and therefore would soon overtake the elevation wave observed at 06:05. The elevation wave was not symmetrical; its back face was steeper (~6:10 a.m. Figure 13 right). This contrasts with the elevation waves we observed without the depression wave superposed, which were either symmetrical or had a steep front face (Figures 9, 11, and 13 left). The steepening of the back face of the elevation wave at 06:10 a.m. suggested that the two waves were superposed so that their vertical velocity signature overlaps.

5. Discussion

The opposite polarity NLIW observed during T1 were of different types compared to the mixed polarity waves observed T2 (see Section 4.2). During T1, the opposite polarity NLIW propagated in separated pycnoclines, and the depression/elevation waves did not modify the near-bed/near-surface isotherm positions (Figure 11b). The buoyancy perturbation was observed at different heights under depression and elevation waves. To describe opposite polarity NLIW, two distinct vertical structure functions are needed and therefore cannot be found with the idealized Equation 3. The opposite polarity NLIW were symmetrical, and the alternating vertical current associated with the NLIW of each polarity was clearly separated and not observed throughout the entire water column (Figure 11b). In contrast, the mixed polarity waves impacted the entire water column (Figure 7f), and were unsymmetrical, and the vertical current of the depression and elevation waves overlapped as they underwent a change in polarity, as shown by Shroyer et al. (2009). In the case of mixed polarity waves, elevation waves are

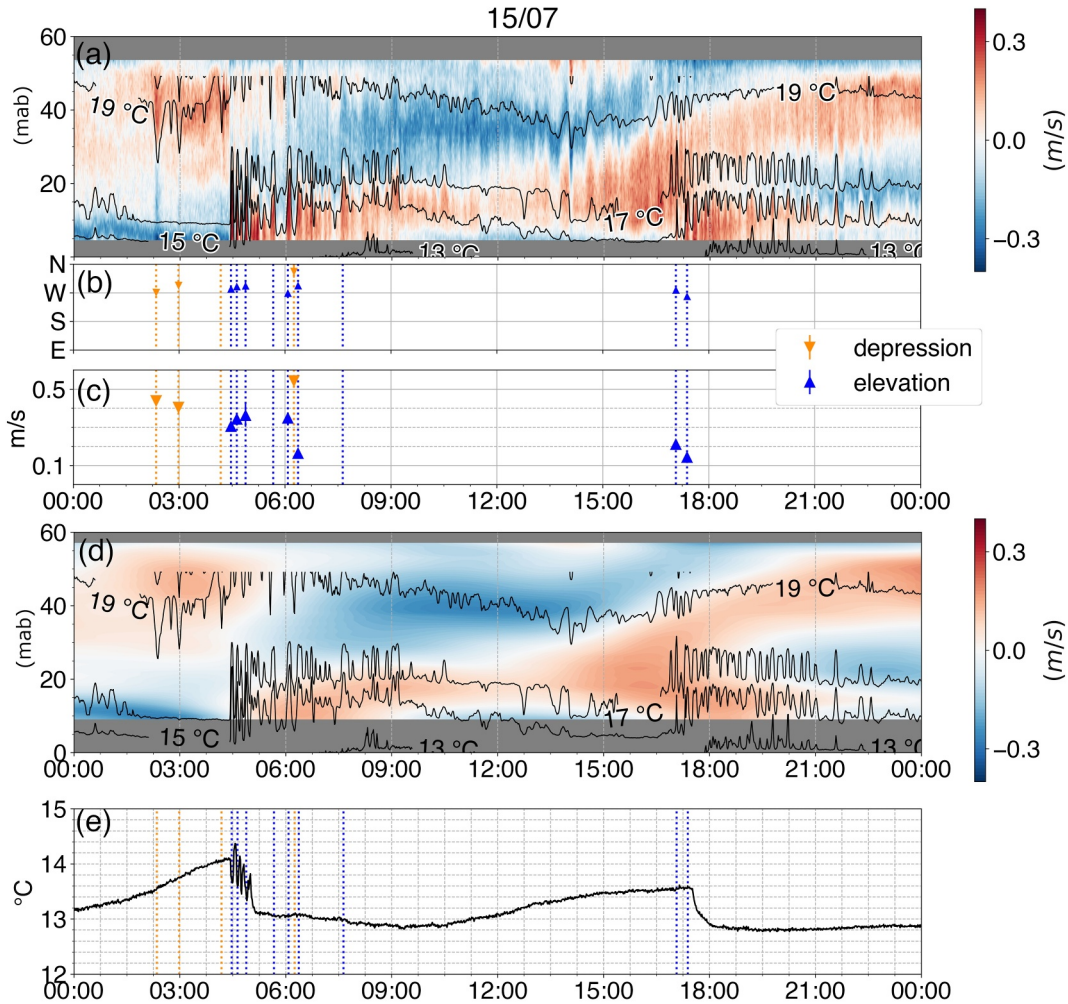

Figure 12. (a) Cross-shore total velocity. (b) Direction of arrival of the NLIW (Blue triangles correspond to the elevation waves, and orange triangles correspond to the depression waves). The dotted line corresponds to the time when an NLIW was observed (orange lines correspond to depressions, and blue lines to elevations). (c) NLIW propagation speed (Blue triangles correspond to the elevation, and orange triangles correspond to the depression). (d) Fast-changing background current (5-hr-low-pass filtered) cross-shore velocity. Note that here cross-shore velocity includes the tidal and subtidal baroclinic currents whereas the velocity in Figure 4 was band-pass filtered and the depth-averaged current was removed. (e) Bottom temperature 70 cm above the seabed (black line).

formed from the depression waves whereas the opposite polarity NLIW are independent. Opposite polarity waves in double pycnoclines have been observed off the Californian coast but have not been highlighted (Cheriton, McPhee-Shaw, Storlazzi, et al., 2014; McSweeney et al., 2020).

The coexistence of mode-1 NLIW of opposite polarity is theoretically possible under some stratification profiles such as double pycnoclines with specific characteristics (Grimshaw et al., 2004; Lamb, 2023). Lamb (2023) found that elevation and depression waves are solutions of the horizontally uniform version of the Dubreil-Jacotin-Long (DJL) equation (i.e., conjugate flow condition) for given double pycnocline stratifications. The position and relative intensity of the three layers defining the double-pycnocline stratification describe a parameter space that specifies the coexistence of depression and elevation DJL waves with conjugate flow. Note that DJL solutions are nonlinear, solitary, steady, and nonviscous waves; therefore, the solutions are of permanent form and can be of higher amplitude than the KdV solitons. Furthermore, only mode-1 waves can be a solution of the DJL equation (Lamb, 2023). DJL waves are not a perfect description of the observed waves, and therefore, it is challenging to verify conjugate flow. However, we can compare the characteristics of the stratification in the parameter space of Lamb (2023) and therefore relate our observations to theory (see Figure 5—(Lamb, 2023)). During T1, given our

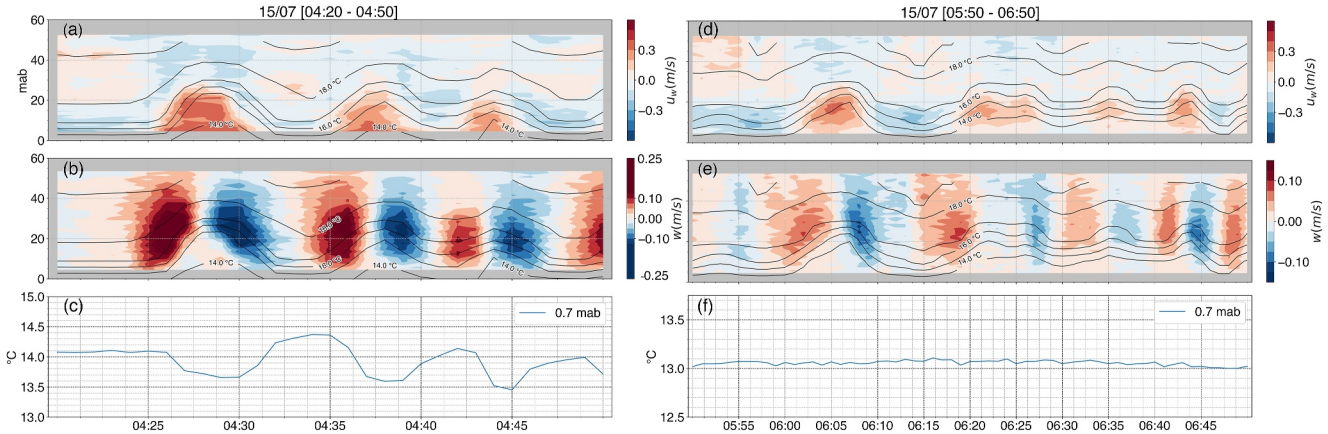

Figure 13. Two examples of NLIW on the 15/07 (left) between 04:20 and 04:50 (right) and between 05:50 and 06:50. Black lines show isotherms every 0.5°C. (a, d) Horizontal residual velocity between the total velocity and the fast-changing background velocity in the mean direction of the wave propagation u_w (color). (b, e) Vertical velocity w. (c, f) Bottom temperature 70 cm above the sea floor.

observed bottom layer thickness (6.2 mab, corresponds to $h_3 = 0.1$ in Lamb's paper), the upper layer thickness (46 mab corresponds to $h_1 = 0.26$ in Lamb's paper) (black stars in Figure 14c), and the ratio of the density difference over the water column, that is, $\Delta\rho_1 = 0.32$ (black stars in Figure 14a), Lamb (2023) predicts the coexistence of DJL NLIW of opposite polarity for an assumed pycnocline thickness of 2.3 m (see Lamb (2023) Figure 5a). During T2, the surface pycnocline was stronger and the bottom pycnocline was uplifted compared to T1 (Figures 14c and 14d). During T2, given the observation of the bottom layer thickness (17 m corresponds to $h_3 = 0.27$ under Lamb's convention, we approximated to 0.3.), the upper thickness (47.7 mab corresponds to $h_1 = 0.27$ in Lamb's paper) (black stars in Figure 14d), and the ratio of the density difference over the water column, that is, $\Delta\rho_1 = 0.58$ (black stars in Figure 14b), Lamb (2023) predicts the absence of DJL NLIW of opposite polarity (see Lamb (2023) Figure 5c). During T2, when we observed polarity reversal, the two pycnoclines were closer to each other compared to T1, which considerably reduced h_2, allowing the coexistence of DJL NLIW of opposite polarity. Our observations are consistent with the theoretical model of Lamb (2023), providing the first in situ validation. However, we note that there is uncertainty in the near-surface and near-bottom pycnocline position and strength due to the low vertical resolution of the moored thermistors as well as the lack of coincident salinity observations.

The formation mechanism of the observed opposite polarity waves remains unclear. Opposite polarity waves can either originate from a different internal tide phase, or they can form on the same bore as the result of internal tide breaking as numerically shown by Dauhajre et al. (2021). Packets of waves of opposite polarity can also form from depression waves propagating on spatially varying stratification (Grimshaw et al., 2004) or from previous wave interaction (Lamb, 2023). The clear observations of elevations waves, only during spring tides, and observations of depression waves during neap tide suggest a distinct formation of the opposite polarity waves in our specific case.

6. Summary and Conclusions

On the Landes inner-shelf site, at 62 m depth, the baroclinic current associated with the internal tide dominated the cross-shelf forcing at the onshore site. The internal tide current was up to three times larger, and the NLIW-induced current was up to five times larger than the barotropic tide current. Regular mode-1 NLIW of elevation and depression were observed. Depression waves were observed under spring and neap tides. Elevation waves were steeper and slower than depression waves. Elevation waves propagated around 0.3 m/s with isotherm displacement up to 24 m. The propagation speeds of the elevation waves were slower than the internal tide phase speed. Depression waves propagated around 0.5 m/s with displacement up to 24 m. At the offshore site, at 153 m depth, the observed NLIW were depression waves of around 20 m amplitude and propagated at 0.96 m/s.

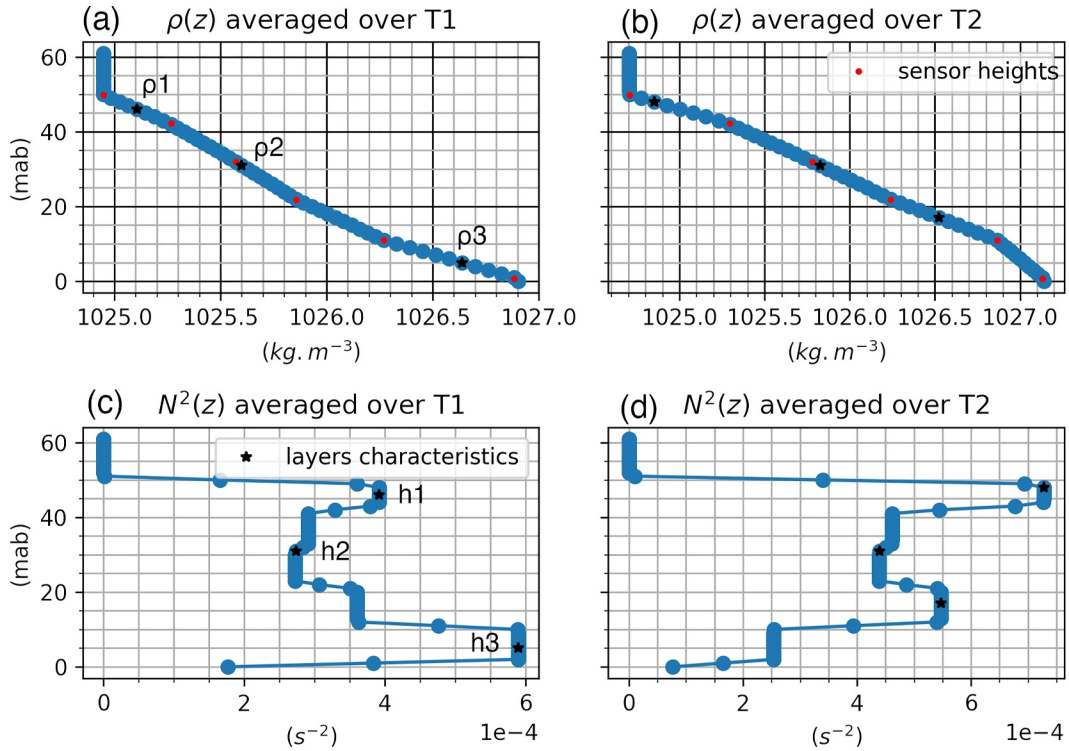

Figure 14. Density (a, b) and associated stratification (c, d) vertical profile. Time-averaged over T1 (a, c) Time-averaged over T2 (b, c). The red points correspond to the sensor heights. The black stars show the characteristics of the three layers that appear in the double-pycnocline stratification profile (surface layer 1 is associated with ρ_1 and h_1, the middle layer 2 is associated with ρ_2 and h_2, and the bottom layer 3 is associated with ρ_3 and h_3).

The inner-shelf NLIW were impacted by variable wind-driven local background dynamics. The observed background stratification was characterized by a double pycnocline that varied in strength and position with the wind forcing. During the second background condition, when the bottom pycnocline was located further from the seabed and the surface pycnocline strengthened and became dominant, offshore NLIW of depression propagated in the near-surface pycnocline and passed through a mixed polarity wave phase as they reversed polarity. Polarity reversal and observation of mixed polarity waves was around the inner-shelf mooring location as they propagated into shallower and more linearly stratified water. During the first background period, there were two pycnoclines at the inner-shelf site with the strongest pycnocline close to the seabed. During most of the first period, we observed canonical bores accompanied by packets of elevation waves that were modulated by the tidal and subtidal currents. The position and intensity of each pycnocline permitted the coexistence of depression and elevation DJL internal solitary waves with conjugate flows (Lamb, 2023). We observed that configuration during three tidal cycles and give a first description of field observation of coexisting waves of opposite polarity. The opposite polarity waves propagated independently along the upper and lower pycnoclines. We showed evidence of superposition between the two waves of opposite polarity.

The coexistence of NLIW of opposite polarity raises the question of interaction and energy transfer (Grimshaw et al., 2004; Lamb, 2023). Grimshaw et al. (2004) numerically demonstrated that the evolution of two depression solitary waves in spatially varying realistic background conditions can lead to interaction between the first solitary wave tail made of elevation waves and the following wave, resulting in weak amplitude modification. Lamb's (2023) numerical study investigated the interaction of DJL solitary waves propagating at different speeds and in the same direction with various combinations of polarity, kinetic energy, and available potential energy. The energy transfer, which resulted in changes in amplitude, propagation speed modification, and the generation of wave packets, was a function of the initial characteristics of the interacting waves (Lamb, 2023). Comparison of Lamb's (2023) results with our time series

observations in an ocean with likely spatially inhomogeneous background conditions is difficult. Cross-shelf observations of interacting waves would enhance our understanding of the impact of inhomogeneous fast-changing background conditions, bottom friction, and nonparallel propagation of the waves. A comparison of the interaction between idealized, nonviscous DJL waves with field observations could help to refine the energy transfer between the waves and hence better understand the fate of the waves and the associated diapycnal mixing. We note that the background and tidal currents may also modify the conditions under which waves of both polarities exist and require further investigation.

Double pycnocline stratification conditions have been observed along the BoB and on different continental shelves (Cheriton, McPhee-Shaw, Storlazzi, et al., 2014; Zulberti et al., 2022). Not every combination of pycnocline relative strength and position can support waves of opposite polarity (Lamb, 2023). We note that double pycnocline stratification, with similar pycnocline strength, can also result in the generation of mode-2 NLIW through resonant interaction (Rayson et al., 2019) or support mode-1 NLIW of depression (Zulberti et al., 2022). This is more likely in deeper shelf water due to the required increased vertical separation between the pycnoclines, but further research is required to understand the conditions that lead to mode-2 or mode-1 NLIW (Lamb, 2023). In shallower shelf waters, the double pycnocline can support opposite polarity waves as demonstrated here, and this dynamic is not geographically unique. Locations where the bottom pycnocline is strengthened by processes such as wind-driven upwelling, as observed by Cheriton, McPhee-Shaw, Storlazzi, et al. (2014), are likely to experience regular opposite polarity wave events. On the BoB, the modification of stratification and the double pycnocline condition we observed in response to the wind stress is likely to be a regular occurrence during summer on this shelf as previous studies have revealed alternating upwelling and downwelling during the summertime on the SE BoB shelf (Batifoulier et al., 2012; Kersalé et al., 2016; Le Boyer et al., 2013; Rubio et al., 2013; Valencia et al., 2004).

In conclusion, our study revealed the existence of opposite polarity waves and suggested potential interaction between the waves. Our observations can be used to motivate numerical modeling efforts to delineate the production and interaction of opposite polarity waves. Deeper understanding of the interactions of opposite polarity waves will enable more accurate predictions of energy transfer and mixing on the continental shelf.

Appendix A

Over the whole month we computed the density field from temperture measurements using the linear relationship obtained from the MVP measurements (Figure A1). Salinity change in time was confined in the near surface during the period of interest (Figure A2).

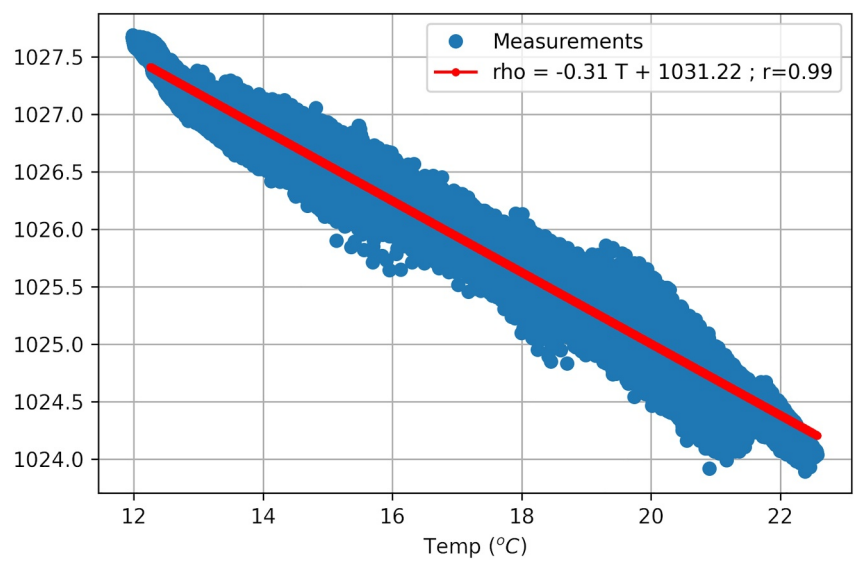

Figure A1. Density as a function of the temperature measured from 3 days of conductivity, temperature, and depth measurements (correspond to 8 transects across the shelf) mounted on the moving vessel profiler (MVP). The red line corresponds to the linear regression with given coefficients. The MVP trajectory is shown in Figure 1.

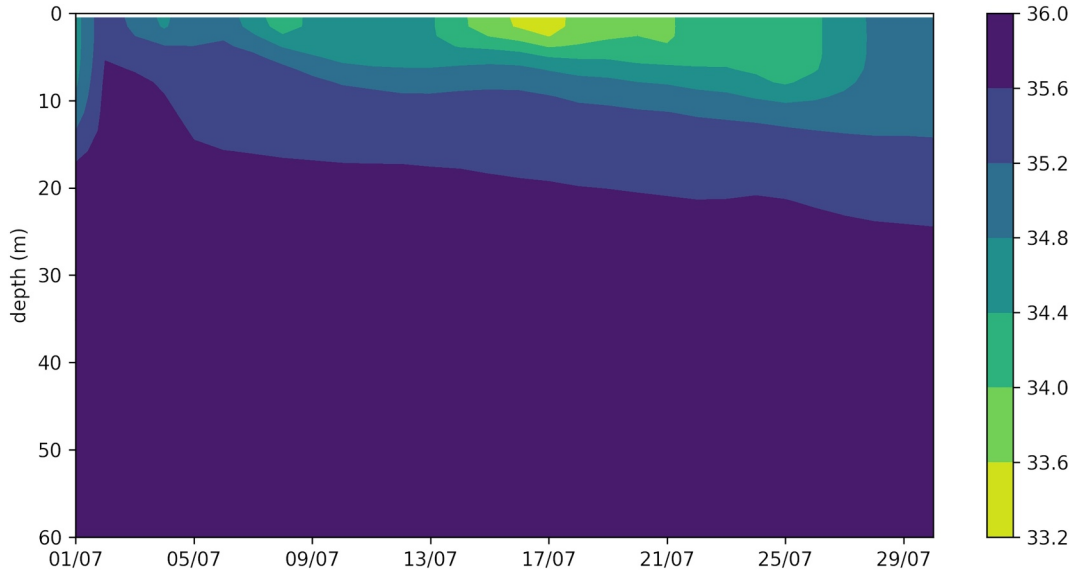

Figure A2. Salinity evolution in time during July 2017 at 44°N, −1.5833232°W (close to the 2C mooring). The data set is from the global ocean eddy-resolving (1/12° horizontal resolution, 50 vertical levels, and daily output) reanalysis GLORYS12V product from Copernicus Marine Service.

Data Availability Statement

Data sets for this research are available in these in-text data citation references: Lazure & Puillat (2017). Such data sets description must be findable and accessible (e.g., via https://doi.org/10.17600/17010800). Data sets is accessible via https://doi.org/10.5281/zenodo.8362896. The gridfit software used for this research is available in these in-text data citation references: D'Errico (2025). Such software must be findable and accessible (e.g., via https://www.mathworks.com/matlabcentral/fileexchange/8998-surface-fitting-using-gridfit).

Acknowledgments

We thank K. Lamb for meaningful discussions on his previous work and the anonymous referees for their examination and suggestions that improved this work. We are grateful for the support of the ISblue project, Interdisciplinary graduate school for the blue planet (ANR-17-EURE-0015) and co-funded by a grant from the French government under the program "Investissements d'Avenir" embedded in France 2030 whose efforts made this research possible. We acknowledge Ifremer PhD scholarship program for the additional funding during A. Moncuquet PhD. This study was partly funded by the Laboratory for Ocean Physics and Satellite remote sensing and Ifremer. Jones and Zulberti were supported by the Australian Research Council (Grants IH200100009, and DP210102745). The ETOILE oceanographic campaign has received funding from the European Commission's Horizon 2020 Research and Innovation program (H2020 JERICO-NEXT). The authors would also like to thank the RV Côte de la Manche crew for their dedicated work as well as the technical team from Ifremer and SHOM for their technical assistance.

References

Azevedo, A., da Silva, J. C. B., & New, A. L. (2006). On the generation and propagation of internal solitary waves in the southern Bay of Biscay. *Deep-Sea Research Part I-Oceanographic Research Papers*, *53*(6), 927–941. https://doi.org/10.1016/j.dsr.2006.01.013

Bai, X., Lamb, K. G., Hu, J., & Liu, Z. (2021). On tidal modulation of the evolution of internal solitary-like waves passing through a critical point. *Journal of Physical Oceanography*, *51*(8), 2533–2552. https://doi.org/10.1175/JPO-D-20-0167.1

Baines, P. G. (1982). On internal tide generation models. *Deep-Sea Research, Part A: Oceanographic Research Papers*, *29*(3), 307–338. https://doi.org/10.1016/0198-0149(82)90098-X

Batifoulier, F., Lazure, P., & Bonneton, P. (2012). Poleward coastal jets induced by westerlies in the Bay of Biscay. *Journal of Geophysical Research*, *117*(C3), C03023. https://doi.org/10.1029/2011JC007658

Charria, G., Lazure, P., Le Cann, B., Serpette, A., Reverdin, G., Louazel, S., et al. (2013). Surface layer circulation derived from Lagrangian drifters in the Bay of Biscay. *Journal of Marine Systems*, *109*, S60–S76. https://doi.org/10.1016/j.jmarsys.2011.09.015

Cheriton, O. M., McPhee-Shaw, E. E., Shaw, W. J., Stanton, T. P., Bellingham, J. G., & Storlazzi, C. D. (2014). Suspended particulate layers and internal waves over the southern Monterey Bay continental shelf: An important control on shelf mud belts? *Journal of Geophysical Research: Oceans*, *119*(1), 428–444. https://doi.org/10.1002/2013JC009360

Cheriton, O. M., McPhee-Shaw, E. E., Storlazzi, C. D., Rosenberger, K. J., Shaw, W. J., & Raanan, B. Y. (2014). Upwelling rebound, ephemeral secondary pycnoclines, and the creation of a near-bottom wave guide over the Monterey Bay continental shelf. *Geophysical Research Letters*, *41*(23), 8503–8511. https://doi.org/10.1002/2014GL061897

Csanady, G. (1981). Circulation in the coastal ocean. *Advances in Geophysics*, *23*, 101–183. https://doi.org/10.1016/S0065-2687(08)60331-3

Dauhajre, D. P., Molemaker, M. J., McWilliams, J. C., & Hypolite, D. (2021). Effects of stratification on shoaling internal tidal bores. *Journal of Physical Oceanography*, *51*(10), 3183–3202. https://doi.org/10.1175/JPO-D-21-0107.1

Davis, K. A., Arthur, R. S., Reid, E. C., Rogers, J. S., Fringer, O. B., DeCarlo, T. M., & Cohen, A. L. (2020). Fate of internal waves on a shallow shelf. *Journal of Geophysical Research: Oceans*, *125*(5), e2019JC015377. https://doi.org/10.1029/2019JC015377

Demerliac, M. A. (1974). Calcul du niveau moyen journalier. *Annales Hydrographiques Du SHOM 5 Éme Série*, 49–57.

D'Errico, J. (2025). *Surface Fitting using gridfit*. MATLAB Central File Exchange. Retrieved from https://www.mathworks.com/matlabcentral/fileexchange/8998-surface-fitting-using-gridfit

Gerkema, T. (1996). A unified model for the generation and fission of internal tides in a rotating ocean. *Journal of Marine Research*, *54*(3), 421–450. https://doi.org/10.1357/0022240963213574

Gerkema, T. (2001). Internal and interfacial tides: Beam scattering and local generation of solitary waves. *Journal of Marine Research*, *59*(2), 227–255. https://doi.org/10.1357/002224001762882646

Ghassemi, A., Zahedi, S., & Boegman, L. (2022). Bolus formation from fission of nonlinear internal waves over a mild slope. *Journal of Fluid Mechanics*, *932*, A50. https://doi.org/10.1017/jfm.2021.1033

Grimshaw, R., Pelinovsky, E., Talipova, T., & Kurkin, A. (2004). Simulation of the transformation of internal solitary waves on oceanic shelves. *Journal of Physical Oceanography*, *34*(12), 2774–2791. https://doi.org/10.1175/JPO2652.1

Grisouard, N., & Staquet, C. (2010). Numerical simulations of the local generation of internal solitary waves in the Bay of Biscay. *Nonlinear Processes in Geophysics*, *17*(5), 575–584. https://doi.org/10.5194/npg-17-575-2010

Helfrich, K. R., & Melville, W. K. (2006). Long non linear internal waves. *Annual Review of Fluid Mechanics*, *38*(1), 395–425. https://doi.org/10.1146/annurev.fluid.38.050304.092129

Jackson, C. R., & Apel, J. R. (2002). Internal Wave Atlas May 2002. Retrieved from https://internalwaveatlas.com/Atlas_index.html

Jackson, C. R., da Silva, J., & Jeans, G. (2012). The generation of nonlinear internal waves. *Oceanography*, *25*(2), 108–123. https://doi.org/10.5670/oceanog.2012.46

Jones, N. L., Ivey, G. N., Rayson, M. D., & Kelly, S. M. (2020). Mixing driven by breaking nonlinear internal waves. *Geophysical Research Letters*, *47*(19), e2020GL089591. https://doi.org/10.1029/2020GL089591

Kersalé, M., Marié, L., Le Cann, B., Serpette, A., Lathuilière, C., Le Boyer, A., et al. (2016). Poleward along-shore current pulses on the inner shelf of the Bay of Biscay. *Estuarine, Coastal and Shelf Science*, *179*, 155–171. https://doi.org/10.1016/j.ecss.2015.11.018

Koutsikopoulos, C., & LeCann, B. (1996). Physical processes and hydrological structures related to the Bay of Biscay anchovy. *Scientia Marina*, *60*(2), 9–19.

Lamb, K. G. (2014). Internal wave breaking and dissipation mechanisms on the continental slope/shelf. *Annual Review of Fluid Mechanics*, *46*(1), 231–254. https://doi.org/10.1146/annurev-fluid-011212-140701

Lamb, K. G. (2023). Interaction of mode-one internal solitary waves of opposite polarity in double-pycnocline stratifications. *Journal of Fluid Mechanics*, *962*, A17. https://doi.org/10.1017/jfm.2023.284

Lazure, P., & Puillat, I. (2017). ETOILE cruise, Côtes De La Manche R/V. Current meters, Subsurface meas. underway (T,S) MVP (Moving vessel profiler) [Dataset]. *Thermistor chain CTD stations*. https://doi.org/10.17600/17010800

Le Boyer, A., Charria, G., Le Cann, B., Lazure, P., & Marié, L. (2013). Circulation on the shelf and the upper slope of the Bay of Biscay. *Continental Shelf Research*, *55*, 97–107. https://doi.org/10.1016/j.csr.2013.01.006

Le Cann, B. (1990). Barotropic tidal dynamics of the Bay of Biscay shelf: Observations, numerical modelling and physical interpretation. *Continental Shelf Research*, *10*(8), 723–758. https://doi.org/10.1016/0278-4343(90)90008-A

Lentz, S. J., & Chapman, D. C. (2004). The importance of nonlinear cross-shelf momentum flux during wind-driven coastal upwelling. *Journal of Physical Oceanography*, *34*(11), 2444–2457. https://doi.org/10.1175/JPO2644.1

Masunaga, E., Arthur, R. S., & Fringer, O. B. (2019). Internal wave breaking dynamics and associated mixing in the coastal ocean. In J. K. Cochran, H. J. Bokuniewicz, & P. L. Yager (Eds.), *Encyclopedia of Ocean Sciences* (3rd ed., pp. 548–554). Academic Press. Retrieved from https://www.sciencedirect.com/science/article/pii/B9780124095489109534

Masunaga, E., Fringer, O. B., Yamazaki, H., & Amakasu, K. (2016). Strong turbulent mixing induced by internal bores interacting with internal tide-driven vertically sheared flow. *Geophysical Research Letters*, *43*(5), 2094–2101. https://doi.org/10.1002/2016GL067812

McSweeney, J. M., Lerczak, J. A., Barth, J. A., Becherer, J., Colosi, J. A., MacKinnon, J. A., et al. (2020). Observations of shoaling nonlinear internal bores across the central California inner shelf. *Journal of Physical Oceanography*, *50*(1), 111–132. https://doi.org/10.1175/JPO-D-19-0125.1

Molinas, E., Carneiro, J. C., & Vinzon, S. (2020). Internal tides as a major process in Amazon continental shelf fine sediment transport. *Marine Geology*, *430*, 106360. https://doi.org/10.1016/j.margeo.2020.106360

New, A. L. (1988). Internal tidal mixing in the Bay of Biscay. *Deep-Sea Research, Part A: Oceanographic Research Papers*, *35*(5), 691–709. https://doi.org/10.1016/0198-0149(88)90026-X

New, A. L., & Pingree, R. D. (1992). Local generation of internal soliton packets in the central bay of Biscay. *Deep-Sea Research, Part A: Oceanographic Research Papers*, *39*(9), 1521–1534. https://doi.org/10.1016/0198-0149(92)90045-U

Ostrovsky, L. A., & Stepanyants, Y. A. (1989). Do internal solitions exist in the ocean? *Reviews of Geophysics*, *27*(3), 293–310. https://doi.org/10.1029/RG027i003p00293

Pairaud, I. (2005). *Modélisation et analyse de la marée interne dans le golfe de Gascogne*. (PhD Thesis). Université Paul Sabatier - Toulouse III. Retrieved from https://tel.archives-ouvertes.fr/tel-00067994

Pichon, A., Morel, Y., Baraille, R., & Quaresma, L. S. (2013). Internal tide interactions in the Bay of Biscay: Observations and modelling. *Journal of Marine Systems*, *109–110*, S26–S44. https://doi.org/10.1016/j.jmarsys.2011.07.003

Pingree, R. D., Mardell, G. T., & New, A. L. (1986). Propagation of internal tides from the upper slopes of the Bay of Biscay. *Nature*, *321*(6066), 154–158. https://doi.org/10.1038/321154a0

Pingree, R. D., & New, A. L. (1989). Downward propagation of internal tidal energy into the Bay of Biscay. *Deep-Sea Research, Part A: Oceanographic Research Papers*, *36*(5), 735–758. https://doi.org/10.1016/0198-0149(89)90148-9

Puillat, I., Lazure, P., Jégou, A. M., Lampert, L., & Miller, P. I. (2004). Hydrographical variability on the French continental shelf in the Bay of Biscay, during the 1990s. *Continental Shelf Research*, *24*(10), 1143–1163. https://doi.org/10.1016/j.csr.2004.02.008

Rayson, M. D., Jones, N. L., & Ivey, G. N. (2019). Observations of large-amplitude mode-2 nonlinear internal waves on the Australian North West shelf. *Journal of Physical Oceanography*, *49*(1), 309–328. https://doi.org/10.1175/JPO-D-18-0097.1

Rubio, A., Fontán, A., Lazure, P., González, M., Valencia, V., Ferrer, L., et al. (2013). Seasonal to tidal variability of currents and temperature in waters of the continental slope, southeastern Bay of Biscay. *Journal of Marine Systems*, *109–110*, S121–S133. https://doi.org/10.1016/j.jmarsys.2012.01.004

Scotti, A., Butman, B., Beardsley, R. C., Alexander, P. S., & Anderson, S. (2005). A modified beam-to-earth transformation to measure short-wavelength internal waves with an acoustic Doppler current profiler. *Journal of Atmospheric and Oceanic Technology*, *22*(5), 583–591. https://doi.org/10.1175/JTECH1731.1

Scotti, A., & Pineda, J. (2004). Observation of very large and steep internal waves of elevation near the Massachusetts coast. *Geophysical Research Letters*, *31*(22), L22307. https://doi.org/10.1029/2004GL021052

Scotti, A., & Pineda, J. (2007). Plankton accumulation and transport in propagating nonlinear internal fronts. *Journal of Marine Research*, *65*(1), 117–145. https://doi.org/10.1357/002224007780388702

Shroyer, E. L., Moum, J. N., & Nash, J. D. (2009). Observations of polarity reversal in shoaling nonlinear internal waves. *Journal of Physical Oceanography*, *39*(3), 691–701. https://doi.org/10.1175/2008JPO3953.1

Shroyer, E. L., Moum, J. N., & Nash, J. D. (2011). Nonlinear internal waves over New Jersey's continental shelf. *Journal of Geophysical Research*, *116*(C3), C03022. https://doi.org/10.1029/2010JC006332

Simon, B. (2007). *La marée océanique côtière*. Institut Océanographique. Retrieved from https://theses.fr/2021TOU30261

Valencia, V., Franco, J., Borja, Á., & Fontán, A. (2004). Chapter 7 - Hydrography of the southeastern Bay of Biscay. In Á. Borja & M. Collins (Eds.), *Elsevier Oceanography Series* (Vol. 70, pp. 159–194). Elsevier. Retrieved from https://www.sciencedirect.com/science/article/pii/S042298940480045X

Vlasenko, V., & Stashchuk, N. (2015). Internal tides near the Celtic Sea shelf break: A new look at a well known problem. *Deep-Sea Research Part I-Oceanographic Research Papers*, *103*, 24–36. https://doi.org/10.1016/j.dsr.2015.05.003

Walter, R. K., Squibb, M., Woodson, C., Koseff, J., & Monismith, S. (2014). Stratified turbulence in the nearshore coastal ocean: Dynamics and evolution in the presence of internal bores. *Journal of Geophysical Research: Oceans*, *119*(12), 8709–8730. https://doi.org/10.1002/2014JC010396

Walter, R. K., Woodson, C. B., Arthur, R. S., Fringer, O. B., & Monismith, S. G. (2012). Nearshore internal bores and turbulent mixing in southern Monterey Bay. *Journal of Geophysical Research*, *117*(C7), C07017. https://doi.org/10.1029/2012JC008115

Walter, R. K., Woodson, C. B., Leary, P. R., & Monismith, S. G. (2014). Connecting wind-driven upwelling and offshore stratification to nearshore internal bores and oxygen variability. *Journal of Geophysical Research: Oceans*, *119*(6), 3517–3534. https://doi.org/10.1002/2014JC009998

Zhang, S., Alford, M. H., & Mickett, J. B. (2015). Characteristics, generation and mass transport of nonlinear internal waves on the Washington continental shelf. *Journal of Geophysical Research: Oceans*, *120*(2), 741–758. https://doi.org/10.1002/2014JC010393

Zulberti, A. P., Jones, N. L., & Ivey, G. N. (2020). Observations of enhanced sediment transport by nonlinear internal waves. *Geophysical Research Letters*, *47*(19), e2020GL088499. https://doi.org/10.1029/2020GL088499

Zulberti, A. P., Jones, N. L., Rayson, M. D., & Ivey, G. N. (2022). Mean and turbulent characteristics of a bottom mixing-layer forced by a strong surface tide and large amplitude internal waves. *Journal of Geophysical Research: Oceans*, *127*(1), e2020JC017055. https://doi.org/10.1029/2020JC017055